

# Intrinsic alignments of galaxies in the MassiveBlack-II simulation: analysis of two-point statistics

Ananth Tenneti<sup>1\*</sup>, Sukhdeep Singh<sup>1†</sup>, Rachel Mandelbaum<sup>1‡</sup>, Tiziana Di Matteo<sup>1§</sup>,  
Yu Feng<sup>1</sup>, Nishikanta Khandai<sup>2,3</sup>

<sup>1</sup>*McWilliams Center for Cosmology, Department of Physics, Carnegie Mellon University, Pittsburgh, PA 15213, USA*

<sup>2</sup>*Department of Physics, Brookhaven National Laboratory, Upton, NY 11973, USA*

<sup>3</sup>*School of Physical Sciences, National Institute of Science Education and Research, Bhubaneswar, Odisha 751005, India*

12 February 2015

## ABSTRACT

The intrinsic alignment of galaxies with the large-scale density field is an important astrophysical contaminant in upcoming weak lensing surveys. We present detailed measurements of the galaxy intrinsic alignments and associated ellipticity-direction (ED) and projected shape ( $w_{g+}$ ) correlation functions for galaxies in the cosmological hydrodynamic MassiveBlack-II (MB-II) simulation. We carefully assess the effects on galaxy shapes, misalignment of the stellar component with the dark matter shape and two-point statistics of iterative weighted (by mass and luminosity) definitions of the (reduced and unreduced) inertia tensor. We find that iterative procedures must be adopted for a reliable measurement of the reduced tensor but that luminosity versus mass weighting has only negligible effects. Both ED and  $w_{g+}$  correlations increase in amplitude with subhalo mass (in the range of  $10^{10} - 6.0 \times 10^{14} h^{-1} M_{\odot}$ ), with a weak redshift dependence (from  $z = 1$  to  $z = 0.06$ ) at fixed mass. At  $z \sim 0.3$ , we predict a  $w_{g+}$  that is in reasonable agreement with SDSS LRG measurements and that decreases in amplitude by a factor of  $\sim 5$ –18 for galaxies in the LSST survey. We also compared the intrinsic alignments of centrals and satellites, with clear detection of satellite radial alignments within their host halos. Finally, we show that  $w_{g+}$  (using subhalos as tracers of density) and  $w_{\delta+}$  (using dark matter density) predictions from the simulations agree with that of non-linear alignment models (NLA) at scales where the 2-halo term dominates in the correlations (and tabulate associated NLA fitting parameters). The 1-halo term induces a scale dependent bias at small scales which is not modeled in the NLA model.

**Key words:** cosmology: theory – methods: numerical – hydrodynamics – gravitational lensing: weak – galaxies: star formation

## 1 INTRODUCTION

Upcoming cosmological surveys such as the Large Synoptic Survey Telescope (LSST)<sup>1</sup>, Euclid<sup>2</sup>, and WFIRST-AFTA<sup>3</sup> have the potential to constrain cosmological parameters such as the dark energy equation of state to percent levels (or better) using weak gravitational lensing. The sensitivity of weak gravitational lensing to both luminous and dark matter

(Benabed & van Waerbeke 2004; Bernstein & Jain 2004; Hu 2002; Huterer 2010; Ishak et al. 2004; Takada & White 2004) makes it a powerful way to probe the nature of dark matter, dark energy and modified theories of gravity (Albrecht et al. 2006; Weinberg et al. 2013). However, the potential to constrain cosmological parameters to sub-percent levels can only be realized if the systematic errors in lensing surveys are even smaller than that.

An important astrophysical systematic that contaminates weak lensing measurements is the intrinsic alignment of galaxies (e.g., Heavens et al. 2000; Croft & Metzler 2000; Jing 2002; Hirata & Seljak 2004). Weak lensing analysis is based on the assumption that the intrinsic shapes and orientations of galaxies are randomly aligned. In reality, the galaxy shapes are correlated with each other and with the underlying density field, mimicking the same coherent shape

\* [vat@andrew.cmu.edu](mailto:vat@andrew.cmu.edu)

† [sukhdees@andrew.cmu.edu](mailto:sukhdees@andrew.cmu.edu)

‡ [rmandelb@andrew.cmu.edu](mailto:rmandelb@andrew.cmu.edu)

§ [tiziana@phys.cmu.edu](mailto:tiziana@phys.cmu.edu)

<sup>1</sup> <http://www.lsst.org/lsst/>

<sup>2</sup> <http://sci.esa.int/euclid/>

<sup>3</sup> <http://wfirst.gsfc.nasa.gov>

alignments that are the signature of weak gravitational lensing. This systematic, called the intrinsic alignment of galaxies, if ignored, can cause a deviation of  $\sim 25\%$  when estimating the dark energy equation of state parameter (Joachimi et al. 2011a). While several schemes for mitigating intrinsic alignments have been proposed, such as nulling (Joachimi & Schneider 2008), self-calibration (Zhang 2010), and joint modeling of cosmological parameters and weak lensing (King 2005, e.g.), the methods that remove the least amount of cosmological information often involve modeling the intrinsic alignments as a function of scale, redshift, luminosity and environment.

The complex nature of the physics of galaxy formation makes it very difficult to model the intrinsic alignments analytically. Popular analytic models include the linear alignment model (Hirata & Seljak 2004), modifications of it based on the non-linear power spectrum (Bridle & King 2007a), and the halo model (Schneider & Bridle 2010), which makes assumptions about the alignment of centrals and satellites. Numerical studies based on  $N$ -body simulations have studied intrinsic alignments by populating the halos with galaxies and assigning a misalignment angle (Heymans et al. 2006) or by using semi-analytic models (Joachimi et al. 2013). In general, methods designed to remove intrinsic alignments from observational data (Joachimi & Schneider 2008, 2009; Bridle & King 2007a; Joachimi & Bridle 2010; Blazek et al. 2012) are based on these models or require accurate redshift information which leads to considerable loss of cosmological information. A further understanding of intrinsic alignments requires the use of cosmological numerical simulations that include the physics of galaxy formation to validate the theoretical predictions.

Here, we make use of a large volume, high-resolution cosmological hydrodynamic simulation, MassiveBlack-II (MB-II) (Khandai et al. 2014) to directly study the intrinsic alignment due to the stellar matter component in galaxies. Recent hydrodynamic simulations of comparable volume that form galaxies include the Horizon-AGN (Dubois et al. 2014) and Illustris (Vogelsberger et al. 2014). In a previous paper (Tenneti et al. 2014), we studied the shapes of stellar matter component in galaxies and their alignment with the shape of the host dark matter subhalo using MassiveBlack-II. We extend this work further in this paper, by studying the two-point correlation functions. This study allow us to both (a) compare our results from MB-II with observational measurements at high luminosity, to validate the use of these simulations for intrinsic alignment studies; and (b) to predict intrinsic alignment signals for lower luminosity galaxies that will be used in upcoming weak lensing surveys.

The intrinsic alignments of galaxies in the simulation are based on the shapes and orientations of stellar matter component in galaxies. The shape of a galaxy is determined by the radial weighting used for measuring the inertia tensor, and also the mass or luminosity weighting given to each star particle while calculating the inertia tensor. We previously studied the distributions of shapes determined by dark matter and stellar matter component in galaxies using the unweighted inertia tensor by weighting each star particle by its mass (Tenneti et al. 2014). Using  $N$ -body simulations, Schneider et al. (2012) found radial dependence in the axis ratios of the shapes of dark matter halos. Bett (2012) studied the axis ratios of dark matter halos in  $N$ -body simula-

tions using different definitions of the inertia tensor. In this paper, we extend our previous work to investigate the dependence of axis ratio distributions of the shapes of stellar matter determined using the unweighted and reduced forms of inertia tensor (defined in Sec. 2.2). We also consider the effect of weighting star particles by their luminosity instead of mass, which is more appropriate for comparison with observations. In addition to studying shape distributions, we check the impact of choices made when calculating the per-galaxy inertia tensor on the predicted intrinsic alignment two-point functions.

The main focus of this paper is the investigation of two-point correlation functions using the shapes of stellar matter component in galaxies. For comparison with previous results based on  $N$ -body simulations, we can study the position angle statistics, while the projected shape correlations are necessary for comparison with many observational results. The position-angle statistics study the correlation of shapes by considering only their orientation. Using  $N$ -body simulations, Lee et al. (2008) and Hopkins et al. (2005) investigated the mass dependence and redshift evolution of the alignment of halos with each other. Due to the mass dependence of the misalignment angle of the shape of stellar matter component of a galaxy with its host subhalo shape, we have to investigate this dependence by using the shapes of stellar matter. Codis et al. (2014) used the Horizon-AGN simulation to understand intrinsic alignments of simulated galaxies at redshift  $z = 1.2$  using the spin of stellar matter component.

As we know both the ellipticity and orientation of stellar matter component in galaxies, it is possible to compute the cross correlations of the projected shapes with each other or the underlying density field statistic. We investigate the mass and redshift dependence of the intrinsic shape-density cross-correlation function in the subhalo mass range of  $10^{11} - 10^{14} h^{-1} M_{\odot}$  and at redshifts  $z = 1.0, 0.3,$  and  $0.06$ . The availability of spectral energy distributions (SED) of star particles in the simulation (Khandai et al. 2014) also allows us to calculate the luminosities of each galaxy in a given band and study intrinsic alignments for galaxy samples selected with a luminosity threshold. It is possible to divide the galaxies in the simulation into centrals and satellites and calculate the intrinsic alignment separately, for comparison in a given mass bin. The dependence of intrinsic alignments on the color of galaxies (red and blue) has been investigated observationally, for example by Hirata et al. (2007) and Mandelbaum et al. (2011). These results indicate larger intrinsic alignments for red galaxies. Here, we will use SEDs to determine colors that we can use to approximately divide our sample of galaxies into red and blue types, to confirm the consistency with the observational findings on the importance of color in determining intrinsic alignments.

This paper is organized as follows. In Section 2, we describe the simulation, MB-II, used in this study and the different methods adopted to obtain the shapes and orientations of the stellar matter component in subhalos. In Section 3, we define the two-point correlation functions analyzed in this paper. In Section 4, we show how the axis ratios and two-point correlation functions depend on the choices made when computing the inertia tensor, while Section 4.4 discusses the effect of using luminosity weighted inertia tensor. In Section 5, we analyze the color dependence

of shapes and two-point correlation functions by dividing the galaxy sample into red and blue types. In Section 6, we investigate the mass and redshift dependence of intrinsic alignment two-point correlation functions. A comparison of intrinsic alignments in centrals and satellites is made in Section 7. In Section 8, we compare our results with observations and make predictions for intrinsic alignments in upcoming weak lensing surveys. Finally, our conclusions are summarized in Section 9. In addition, we also provide fitting functions for the intrinsic alignment signals in different mass and luminosity bins at different redshifts in Appendix A.

## 2 METHODS

### 2.1 MassiveBlack-II Simulation

In this study, we used the MassiveBlack-II (MB-II) hydrodynamic simulation to predict the intrinsic alignment of the shapes of stellar matter component in galaxies. MB-II is a state-of-the-art high resolution, large volume, cosmological hydrodynamic simulation of structure formation. This simulation has been performed with P-GADGET, which is a hybrid version of the parallel code, GADGET2 (Springel et al. 2005) upgraded to run on Petaflop scale supercomputers. In addition to gravity and smoothed-particle hydrodynamics (SPH), the P-GADGET code also includes the physics of multiphase ISM model with star formation (Springel & Hernquist 2003), black hole accretion and feedback (Springel et al. 2005; Di Matteo et al. 2012). Radiative cooling and heating processes are included (as in Katz et al. 1996), as is photoheating due to an imposed ionizing UV background. The details of this simulation can be found in Khandai et al. (2014).

MB-II contains  $N_{\text{part}} = 2 \times 1792^3$  dark matter and gas particles in a cubic periodic box of length  $100h^{-1}\text{Mpc}$  on a side, with a gravitational smoothing length  $\epsilon = 1.85h^{-1}\text{kpc}$  in comoving units. A single dark matter particle has a mass  $m_{\text{DM}} = 1.1 \times 10^7 h^{-1} M_{\odot}$  and the initial mass of a gas particle is  $m_{\text{gas}} = 2.2 \times 10^6 h^{-1} M_{\odot}$ , with the mass of each star particle being  $m_{\text{star}} = 1.1 \times 10^6 h^{-1} M_{\odot}$ . The cosmological parameters used in the simulation are as follows: amplitude of matter fluctuations  $\sigma_8 = 0.816$ , spectral index  $\eta_s = 0.96$ , mass density parameter  $\Omega_m = 0.275$ , cosmological constant density parameter  $\Omega_{\Lambda} = 0.725$ , baryon density parameter  $\Omega_b = 0.046$ , and Hubble parameter  $h = 0.702$  as per WMAP7 (Komatsu et al. 2011).

Halo catalogs of particles in the simulation are generated using the friends of friends (FoF) halo finder algorithm (Davis et al. 1985). The FoF algorithm identifies halos on the fly using a linking length of 0.2 times the mean interparticle separation. The subhalo catalogs are generated using the SUBFIND code (Springel et al. 2001) on the halo catalogs. The subhalos are defined as locally overdense, self-bound particle groups. In this paper, we will be concerned with the analysis of shapes and their two-point correlation functions. Groups of particles are identified as subhalos if they have at least 20 gravitationally bound particles; however, based on convergence tests in Tenneti et al. (2014), we only use their measured shapes if there are  $\geq 1000$  particles. In this paper, we identify the galaxies to be the subhalos and only consider the shape defined by the stellar component while computing 1-point and 2-point statistics as it is directly relevant to

observational measurements. A comparison of the properties of galaxies identified by different subfinder codes (such as Subfind, Structure finder, etc.) in cosmological simulations that include baryonic physics can be found in Knebe et al. (2013). They find that various galaxy properties agree among the different subfinder codes. However, the impact on shapes in high resolution cosmological simulations is not investigated yet.

### 2.2 Shapes of galaxies and dark matter halos

In this section, we give the details of the different methods adopted to find the shape defined by the dark matter and stellar matter component in subhalos. We model the shapes of the dark matter and stellar matter components of subhalos as ellipsoids in three dimensions by using the eigenvalues and eigenvectors of the inertia tensor, which describes the mass or luminosity distribution. In the interest of comparison with observations, we also project the halos and subhalos onto the  $XY$  plane and model the shapes as ellipses. These are needed to compute projected shape correlation functions, which we will define in Sec. 3.2. In 3D, consider the eigenvectors of the inertia tensor to be  $\hat{e}_a, \hat{e}_b, \hat{e}_c$  with the corresponding eigenvalues being  $\lambda_a, \lambda_b, \lambda_c$ , where  $\lambda_a > \lambda_b > \lambda_c$ . The eigenvectors represent the principal axes of the ellipsoid with the lengths of the principal axes  $(a, b, c)$  given by the square roots of the eigenvalues  $(\sqrt{\lambda_a}, \sqrt{\lambda_b}, \sqrt{\lambda_c})$ . The 3D axis ratios are defined as

$$q = \frac{b}{a}, \quad s = \frac{c}{a} \quad (1)$$

In 2D, the eigenvectors are  $\hat{e}'_a, \hat{e}'_b$  with the corresponding eigenvalues  $\lambda'_a, \lambda'_b$ , where  $\lambda'_a > \lambda'_b$ . The lengths of major and minor axes are  $a' = \sqrt{\lambda'_a}$ ,  $b' = \sqrt{\lambda'_b}$  with axis ratio  $q' = \frac{b'}{a'}$ .

We explore several different ways of computing the inertia tensor based on the mass or luminosity, and the radial weighting given to each particle. The unweighted inertia tensor (used for all results in Tenneti et al. 2014) is given by

$$I_{ij} = \frac{\sum_n m_n x_{ni} x_{nj}}{\sum_n m_n}, \quad (2)$$

where  $m_n$  represents the mass of the  $n^{\text{th}}$  particle and  $x_{ni}, x_{nj}$  represent the position coordinates of the  $n^{\text{th}}$  particle with  $0 \leq i, j \leq 2$  in 3D and  $0 \leq i, j \leq 1$  in 2D. Here all particles are given equal weight irrespective of their distance from the center of a subhalo. We can also use the reduced inertia tensor, which gives more weight to particles which are closer to the center:

$$\tilde{I}_{ij} = \frac{\sum_n m_n \frac{x_{ni} x_{nj}}{r_n^2}}{\sum_n m_n} \quad (3)$$

where

$$r_n^2 = \sum_i x_{ni}^2 \quad (4)$$

Unlike for  $N$ -body simulations where it is natural to let each equally-weighted dark matter particle contribute equally to the inertia tensor, for simulated galaxies it is natural to consider weighting each particle by its luminosity, considering that flux is what we actually see when we observe the galaxy. This results in another definition for the

inertia tensor:

$$I_{ij}^{(\text{lum})} = \frac{\sum_n l_n x_{ni} x_{nj}}{\sum_n l_n}, \quad (5)$$

where each stellar particle is weighted by its luminosity,  $l_n$  instead of its mass. The definition presented here refers to the luminosity-weighted form of unweighted inertia tensor given in Eq. 2. In our analysis, we also use the shapes obtained using the luminosity-weighted form of reduced inertia tensor (Eq. 3) defined analogously.

Instead of determining axis ratios with a single calculation, we can also adopt iterative methods for finding the shapes using unweighted and reduced inertia tensors. In the unweighted iterative and reduced iterative methods, we first determine the axis ratios by the standard definitions of the corresponding inertia tensors using all the particles of a given type in the subhalo. Keeping the enclosed volume constant (as in Schneider et al. 2012), the lengths of the principal axes of ellipsoids are rescaled accordingly<sup>4</sup>. After this rescaling, we determine the shapes again, discarding particles outside the ellipsoidal volume. This process is repeated until convergence is reached. Our convergence criterion is that the fractional change in axis ratios must be below 1%. It is to be noted here that although we only use subhalos that initially have at least 1000 dark matter and star particles to calculate shapes, the use of iterative methods results in some low mass subhalos having fewer than 1000 particles in the enclosed volume. But, since this is a very low fraction (less than 0.5%) and the number of particles remaining is very close to 1000, we include them for further analysis.

We will investigate the dependence of using these different definitions on the probability distributions of axis ratios and the two-point correlation functions. Having outlined the differences, we will present the rest of our predictions from the simulation based on the reduced iterative inertia tensor alone.

### 2.3 Misalignment angle

To study the relative orientation between the shapes defined by dark matter and stellar matter component in subhalos, we compute the probability distributions of misalignment angles as in Tenneti et al. (2014). Let  $\hat{e}_{da}$  and  $\hat{e}_{ga}$  be the major axes of the shapes defined by dark matter and stellar matter components respectively. We can then define the misalignment angle by

$$\theta_m = \arccos(|\hat{e}_{da} \cdot \hat{e}_{ga}|). \quad (6)$$

## 3 TWO-POINT CORRELATION FUNCTIONS

Here we define the intrinsic alignment two-point correlation functions that we use in this work. Intrinsic alignments can arise due to the correlation of intrinsic shapes of galaxies with each other (II term) or the correlation of the gravitational shear and intrinsic ellipticity (GI term). The two-point statistics discussed in this paper concern the GI term.

<sup>4</sup> Note that some authors instead keep the length of the major axis fixed (e.g., Allgood et al. 2006; Bett 2012)

### 3.1 Position angle statistics

The position angle statistics, Ellipticity-Ellipticity (EE) and Ellipticity-Direction (ED) correlation functions, are useful to quantify the correlations between the position angles of galaxies or halos with each other and with the large-scale density field as a function of mass and redshift. These can then be compared against results for halos in  $N$ -body simulations. We follow the notation of Lee et al. (2008) to define the EE and ED correlations.

If  $\hat{e}_a(\mathbf{x})$  is the direction of the major axis of the shape of the dark matter or stellar matter component of a subhalo centered at position  $\mathbf{x}$ , then the EE correlation function in 3D,  $\eta(r)$ , is given by

$$\eta(r) = \langle |\hat{e}_a(\mathbf{x}) \cdot \hat{e}_a(\mathbf{x}+\mathbf{r})|^2 \rangle - \frac{1}{3}. \quad (7)$$

Here,  $\langle \cdot \rangle$  means an average over pairs of galaxies separated by a distance,  $r$ . For galaxies or halos randomly oriented according to a uniform distribution, the expectation value of this quantity is zero.

The ED correlation function cross-correlates the orientation of the major axis of the shape of a subhalo with the large-scale density field. For a subhalo centered at position  $\mathbf{x}$  with major axis direction  $\hat{e}_a$ , let the unit vector in the direction of the tracer of the matter density field at a distance  $r$  be  $\hat{\mathbf{r}} = \mathbf{r}/r$ . Then the ED cross-correlation function is given by

$$\omega(r) = \langle |\hat{e}_a(\mathbf{x}) \cdot \hat{\mathbf{r}}(\mathbf{x})|^2 \rangle - \frac{1}{3} \quad (8)$$

which is again zero in the case of no intrinsic alignments.

We can represent the tracers of the matter density field using either the positions of dark matter particles (in which case the correlation function is denoted by the symbol  $\omega_\delta$ ) or the positions of subhalos (in which case it includes a factor of the subhalo bias, and is simply denoted  $\omega$ ).

### 3.2 Projected shape correlation functions

The projected shape correlation functions are computed to directly compare our results from simulations with observations. Here, we follow the notation of Mandelbaum et al. (2006) to give formulae for the calculation of galaxy-intrinsic shear correlation function ( $\hat{\xi}_{g+}(r_p, \Pi)$ ) and the projected statistic,  $w_{g+}$ . Here,  $r_p$  is the comoving transverse separation of a pair of galaxies in the  $XY$  plane and  $\Pi$  is their separation along the  $Z$  direction.

If  $q' = \frac{b'}{a'}$  is the axis ratio of the projected shape of the dark matter or stellar matter component of a subhalo and  $\phi$  is the position angle of the major axis of the ellipse, the components of the ellipticity are given by

$$(e_+, e_\times) = \frac{1 - q'^2}{1 + q'^2} [\cos(2\phi), \sin(2\phi)], \quad (9)$$

where  $e_+$  refers to the radial component of ellipticity and  $e_\times$  is the component at  $45^\circ$  rotation. The galaxy-intrinsic shear correlation function cross-correlates the ellipticity of galaxies with the density field. The ‘‘shape sample’’ denoted by  $S_+$  is selected on the basis of a threshold or binning in subhalo mass, stellar mass, band luminosity and other properties of the galaxies in the simulation, while all the subhalos

are used to trace the density field, forming a “density sample” denoted by  $D$ . The cross-correlation function is then computed using

$$\hat{\xi}_{g+}(r_p, \Pi) = \frac{S_+D - S_+R}{RR} \quad (10)$$

where  $r_p$  is the transverse separation of the galaxy points and  $\Pi$  is the radial red-shift space separation (here, it is the separation along the  $Z$  direction), and  $S_+D$  is the sum over all pairs with separations  $r_p$  and  $\Pi$ :

$$S_+D = \sum_{i \neq j | r_p, \Pi} \frac{e_+(j|i)}{2\mathcal{R}}, \quad (11)$$

where  $e_+(j|i)$  is the + component of the ellipticity of a galaxy ( $j$ ) from the shear sample relative to the direction of a tracer of density field ( $i$ ) selected from the density sample. Here,  $\mathcal{R} = (1 - e_{rms}^2)$  is the shear responsivity that converts from distortion to shear with  $e_{rms}$ , the rms ellipticity per component of the shape sample. Alternatively, we can also define the ellipticity by  $e = \frac{1-q'}{1+q'}$ , in which case we do not have to take the responsivity correction into account. However, using this definition decreases the intrinsic alignment signal by only about  $\sim 6\%$ . So, in the rest of this paper, we employ the former definition as it makes it easier for comparison with observations.  $S_+R$  is defined by a similar equation for the correlation of the data sample with a random density field distribution to remove observational systematics in the shear estimates, and hence we can neglect this term here. The projected correlation function,  $w_{g+}(r_p)$  is now given by

$$w_{g+}(r_p) = \int_{-\Pi_{\max}}^{+\Pi_{\max}} \hat{\xi}_{g+}(r_p, \Pi) d\Pi \quad (12)$$

We calculated the correlation functions over the whole length of the box ( $100h^{-1}\text{Mpc}$ ) with  $\Pi_{\max} = 50h^{-1}\text{Mpc}$ , in 25 bins of size  $4h^{-1}\text{Mpc}$  each. The projected correlation functions are obtained by summing over the galaxy-intrinsic and intrinsic-intrinsic shear correlation functions with the integrand replaced by a summation. Note that the  $w_{g+}$  signal can also be calculated using projected shapes along some other plane instead of XY. However, we did not observe significant differences in the signal for  $w_{g+}(r_p)$  calculated by projecting along YZ and XZ planes. Thus, all reported results use shapes projected on the XY plane.

An alternative way to trace the density field for the calculation of  $w_{g+}$  is to use the positions of all dark matter particles in the simulation instead of subhalos. The correlation function obtained in this way is denoted by  $w_{\delta+}$ . The former is what we can compare with observations, but we can use the latter to test the standard conversion that is used between the two (dividing the observational signals by the linear galaxy bias).

The observable,  $w_{g+}$  is related to the GI term which is discussed further in the section below. We do not discuss the intrinsic shear-shear correlation functions, ( $\hat{\xi}_{++}(r_p, \Pi)$ ,  $\hat{\xi}_{\times\times}(r_p, \Pi)$ ) and their corresponding projected statistics, ( $w_{++}$ ,  $w_{\times\times}$ ) in this paper due to their being extremely noisy. Moreover, it has been shown in multiple theoretical studies (e.g., Hirata & Seljak 2004) that if intrinsic alignments are caused by something like the tidal alignment model, the  $\Pi$

contamination to cosmic shear signals will be quite subdominant to the GI contamination. Given that all measurements to date of strong intrinsic alignments on large scales have been made with red galaxies, and are consistent with the tidal alignment model (e.g., Blazek et al. 2011), we mainly focus on the GI-type intrinsic alignment contamination here. As a practical matter, there is additional motivation to focus on measuring  $w_{g+}$  rather than  $w_{++}$ , because for alignments consistent with the tidal alignment model, the signal-to-noise ratio for the former will be higher than for the latter (see section 4.1 of Singh et al. 2014). Finally, for this type of alignment, measurements of GI provide a unique prediction for  $\Pi$ , so our measurements are equally informative about both given that they appear completely consistent with the tidal alignment.

### 3.3 Formalism: Linear Alignment Model

The linear alignment model is the standard formalism used to study intrinsic alignments of galaxy shapes at large scales (Catelan et al. 2001; Hirata & Seljak 2004; Blazek et al. 2011; Chisari & Dvorkin 2013). The observational measurements of intrinsic alignments on large scales can be reproduced using this model. In this section, we briefly describe the main features of the model.

The linear alignment model is based on the assumption that the intrinsic shear of galaxies is determined by the tidal field at the time of formation of the galaxy (assumed to be during matter domination, Catelan et al. 2001). Thus we can write the intrinsic shear in terms of the primordial potential as

$$\gamma^I = (\gamma_+^I, \gamma_\times^I) = -\frac{C_1}{4\pi G} (\partial_x^2 - \partial_y^2, \partial_x \partial_y) \phi_p \quad (13)$$

Hirata & Seljak (2004) derived the 2-point matter-intrinsic alignments power spectra, relating them to the linear matter power spectrum,  $P_\delta^{\text{lin}}$

$$P_{g+}(\vec{k}, z) = A_I b \frac{C_1 \rho_{\text{crit}} \Omega_m}{D(z)} \frac{k_x^2 - k_y^2}{k^2} P_\delta^{\text{lin}}(\vec{k}, z) \quad (14)$$

$$P_{++}(\vec{k}, z) = \left( A_I \frac{C_1 \rho_{\text{crit}} \Omega_m}{D(z)} \frac{k_x^2 - k_y^2}{k^2} \right)^2 P_\delta^{\text{lin}}(\vec{k}, z) \quad (15)$$

$$P_{g\times}(\vec{k}, z) = A_I b \frac{C_1 \rho_{\text{crit}} \Omega_m}{D(z)} \frac{k_x k_y}{k^2} P_\delta^{\text{lin}}(\vec{k}, z) \quad (16)$$

Following Joachimi et al. (2011b), we fix  $C_1 \rho_{\text{crit}} = 0.0134$  and use the arbitrary constant  $A_I$  to describe the amplitude of intrinsic alignments for different samples.  $D(z)$  is the linear growth factor, normalized to unity at  $z = 0$ .

Bridle & King (2007b) suggested using the full non-linear matter power spectrum  $P_\delta^{\text{nl}}$  in Eq. (14) to extend the linear alignment model to quasi-linear scales. This model is called the non-linear linear alignment model (NLA). In this work, we will use the non-linear matter power spectrum generated with the CAMB software (Lewis & Bridle 2002), with a fixed WMAP7 cosmology (Hinshaw et al. 2013).

Fourier transforming Eq. (14) and integrating over line of sight separation  $\Pi$ , we get the two point correlation func-

tion

$$w_{g+}(r_p) = \frac{A_I b_D C_1 \rho_{\text{crit}} \Omega_m}{\pi^2} \int dz \frac{W(z)}{D(z)} \int_0^\infty dk_z \int_0^\infty dk_\perp \frac{k_\perp^3}{(k_\perp^2 + k_z^2) k_z} P_\delta^{\text{nl}}(\vec{k}, z) \sin(k_z \Pi_{\text{max}}) J_2(k_\perp r_p) (1 + \beta \mu^2) \quad (17)$$

$b_D$  is the bias for density sample,  $\mu = k_z/k$  and  $\beta$  is the linear redshift distortion parameter with  $(1 + \beta \mu^2)$  accounting for the effects of redshift-space distortions (RSD, Kaiser 1987; Singh et al. 2014).  $\beta(z) = f(z)/b$ , where  $f(z)$  is the logarithmic growth rate at redshift  $z$ ; in  $\Lambda$ CDM,  $f(z) \sim \Omega_m(z)^{0.55}$ .  $w_{g+}$  is expected to be zero by symmetry.

#### 4 THE IMPACT OF USING DIFFERENT INERTIA TENSOR DEFINITIONS

In this section, we compare the axis ratio distributions and misalignment angle distributions (as presented in Tenneti et al. 2014) when using the different definitions of inertia tensor defined in Sec. 2.2. We also consider how the two-point correlation functions vary when using different shape definitions. For convenience, we define three mass bins based on total subhalos mass, M1 ( $10^{10.0} - 10^{11.5} h^{-1} M_\odot$ ), M2 ( $10^{11.5} - 10^{13.0} h^{-1} M_\odot$ ), and M3 ( $> 10^{13.0} h^{-1} M_\odot$ ).

##### 4.1 Axis ratio distributions

Here, we compare the axis ratios of shapes obtained using different definitions of inertia tensor. In Figs. 1 and 2, we show the histograms of the axis ratios of the 3D shapes of dark matter (Fig. 1) and stellar (Fig. 2) matter components in subhalos using four inertia tensor calculations: unweighted and reduced, non-iterative and iterative. We considered mass bins M1, M2 and M3 with 38768, 8438, and 267 galaxies, respectively. From the plots, we can see that the axis ratio distributions obtained with non-iterative and iterative unweighted inertia tensors are essentially identical. For the reduced inertia tensor, the results for the iterative calculation are uniformly more flattened than for the non-iterative calculation. The reason for this is that the non-iterative reduced calculation implicitly imposes spherical symmetry (via the  $1/r^2$  weighting), which will result in an overly-rounded shape estimate. For this reason, we do not consider the reduced non-iterative calculation to be useful.

Comparing the iterative reduced vs. unweighted results, the axis ratios of dark matter subhalos are slightly larger (rounder) when using the reduced inertia tensor than when using the unweighted one. This finding agrees qualitatively with the findings of Bett (2012) using  $N$ -body simulations. Additionally, the inclusion of baryonic physics in hydrodynamic simulations can lead to more round dark matter shapes in the inner regions of subhalos (e.g., Kazantzidis et al. 2006; Bryan et al. 2013). In future work, we will directly study the impact of baryonic physics on the shapes determined by reduced inertia tensor by comparing our results on shape distributions with those obtained with a dark matter only simulation.

When considering the stellar shapes, we see that the histograms of intermediate-to-major axis ratio,  $q$  ( $\frac{b}{a}$ ), indicate a slight increase for the reduced inertia tensor compared to

shapes obtained from the unweighted tensor, while the histograms of minor-to-major axis ratio,  $s$  ( $\frac{c}{a}$ ), show a decrease in axis ratio. Thus the shape distributions with the reduced inertia tensor are more oblate than the ones with the unweighted inertia tensor. In a previous study (Tenneti et al. 2014), we found that the projected shapes of stellar matter determined using the unweighted inertia tensor are slightly smaller, but compare favorably with observational measurements using the RMS ellipticity statistic. We note here that the projected shapes with reduced inertia tensor will have a smaller value of the RMS ellipticity statistic.

##### 4.2 Misalignment angle distributions

In Fig. 3, we plot the normalized histograms of misalignment angles between the shapes defined by dark matter and stellar matter component in subhalos. The plots show that there is no significant difference in misalignments if we adopt an iterative or non-iterative definition of shape tensor, for both unweighted and reduced cases. For the unweighted inertia tensor, this result is consistent with the distribution of axis ratios in Sec. 4.1, where the histograms are similar for unweighted non-iterative and iterative definitions. For the shapes obtained using the reduced inertia tensor, the histograms of misalignment angles seem to indicate that while the axis ratios change significantly, the relative shape orientation is not altered much. Comparing misalignment histograms obtained using unweighted and reduced inertia tensor, we observe that in the lowest mass bin, M1, the misalignments are slightly smaller if we use the reduced inertia tensor to define shapes, while they are slightly higher in mass bins M2 and M3.

##### 4.3 Two-point correlation functions

Here, we consider the dependence of the intrinsic alignment two-point correlation functions for the shapes of the stellar matter component in subhalos using different definitions of inertia tensor. For both ED and  $w_{g+}$  correlation functions, the errors bars shown in the plots are obtained using the jackknife variance.

In Fig. 4, we show the ED correlation function,  $\omega(r)$ , for the shapes of the stellar matter component for subhalo mass thresholds of  $10^{11} h^{-1} M_\odot$ ,  $10^{12} h^{-1} M_\odot$ , and  $10^{13} h^{-1} M_\odot$ . Similar to the histograms of misalignment angles, the position-angle correlation functions are the same when we use iterative or non-iterative definitions of inertia tensor. The correlation functions are noticeably smaller if we use the reduced inertia tensor to define the shape for all the mass thresholds.

In Fig. 5, we show the projected shape correlation function,  $w_{g+}(r)$ , in different mass bins. We do not observe any significant difference in the correlation function if we use the non-iterative vs. iterative unweighted inertia tensor to define shape. This is consistent with histograms of axis ratios, misalignment angles and the ED correlation function shown before. Going to the reduced definition of inertia tensor, it can be seen that  $w_{g+}$  is smaller for the shapes obtained from iterative reduced inertia tensor. This is expected due to the lower ellipticities (or higher axis ratios) obtained using the reduced inertia tensor. The values of  $w_{g+}$  for the reduced

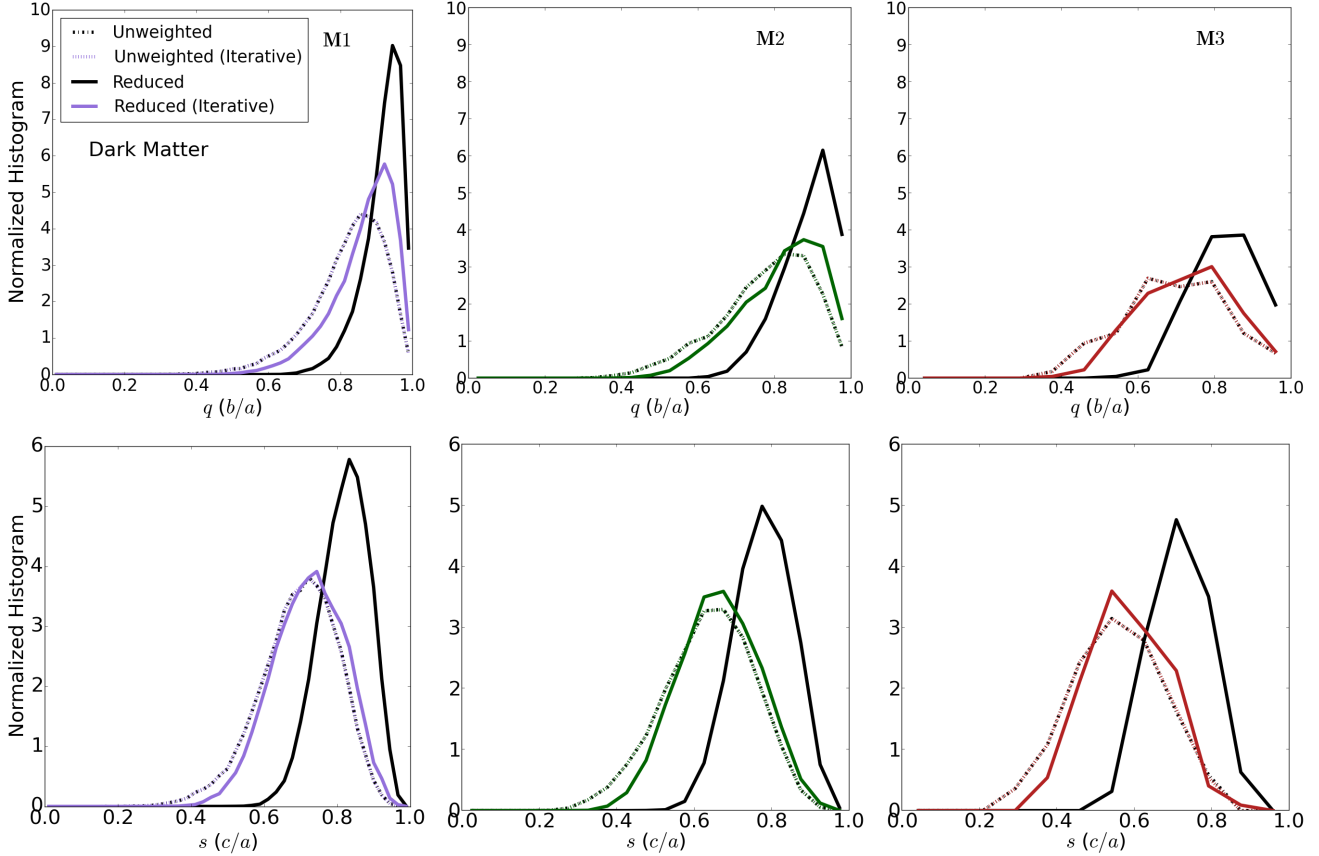


**Figure 1.** Normalized histograms of 3D axis ratios of dark matter component in subhalos using different definitions of inertia tensor in mass bins M1, M2 and M3 at  $z = 0.3$ . The number of galaxies are 38768, 8438, and 267 respectively in mass bins M1, M2 and M3. *Top:*  $q (b/a)$ ; *Bottom:*  $s (c/a)$ .

non-iterative shape tensor are even smaller due to the very high axis ratios, however as mentioned previously we do not consider this a viable way of measuring shapes.

Our analysis presented in this section shows that the results from the unweighted non-iterative inertia tensor are quite similar to those obtained using the iterative tensor, so we do not have to consider this option separately. It is fair to not consider the results obtained using non-iterative reduced inertia tensor due to the expectation that it will produce overly round shapes. Based on these conclusions, our further analysis is based on the shapes obtained using only the iterative versions of unweighted and reduced inertia tensors

#### 4.4 Shapes determined using luminosity weighting

In this section, we investigate the effect of weighting each stellar particle by its luminosity instead of mass while computing the inertia tensor. For the unweighted inertia tensor, we follow Eq. 5; the reduced form of the luminosity weighted inertia tensor can be inferred from it in a straight-forward manner. For each star particle, we use the SDSS  $r$ -band luminosity from the simulation, and determine shapes iteratively.

In Fig. 6, we show the histograms of axis ratios (in the M2 mass bin) of stellar matter in subhalos, computed using both the mass- and luminosity-weighted form for the un-

weighted and reduced inertia tensor. From the plot, we can see that there is no major change in the distribution of axis ratios due to luminosity weighting for the unweighted inertia tensor. The histograms of axis ratios obtained from the reduced inertia tensor show that the luminosity weighting leads to larger values of  $q (b/a)$  and smaller values of  $s (c/a)$ . Thus, the overall shapes are more oblate when using luminosity weighting. This is expected as the mass to light ratio is not constant in the inner regions of the subhalos.

Likewise, we can infer from the left panel of Fig. 7 that luminosity weighting has no effect on the distribution of misalignment angles in the unweighted case, while the stellar shapes obtained from reduced luminosity weighting are more misaligned with the shapes of their host dark matter subhalos. The middle panel of the same figure shows the ED correlation function,  $\omega(r)$ , and the right panel shows the plot of  $w_{g+}(r)$ . In the bottom panels, we plot the ratio of the ED and  $w_{g+}$  signals obtained using the mass weighted inertia tensor with the ones using luminosity weighted tensor. Both the plots indicate that the amplitude and shape of correlation functions obtained using luminosity-weighted shapes are consistent with the ones obtained using mass-weighted shapes. Similarly, at other mass thresholds, the effect of luminosity weighting on correlation functions is not very significant. Although the histograms of shapes and misalignment angles obtained by using the reduced form of luminosity weighted inertia tensor are different, we do not observe

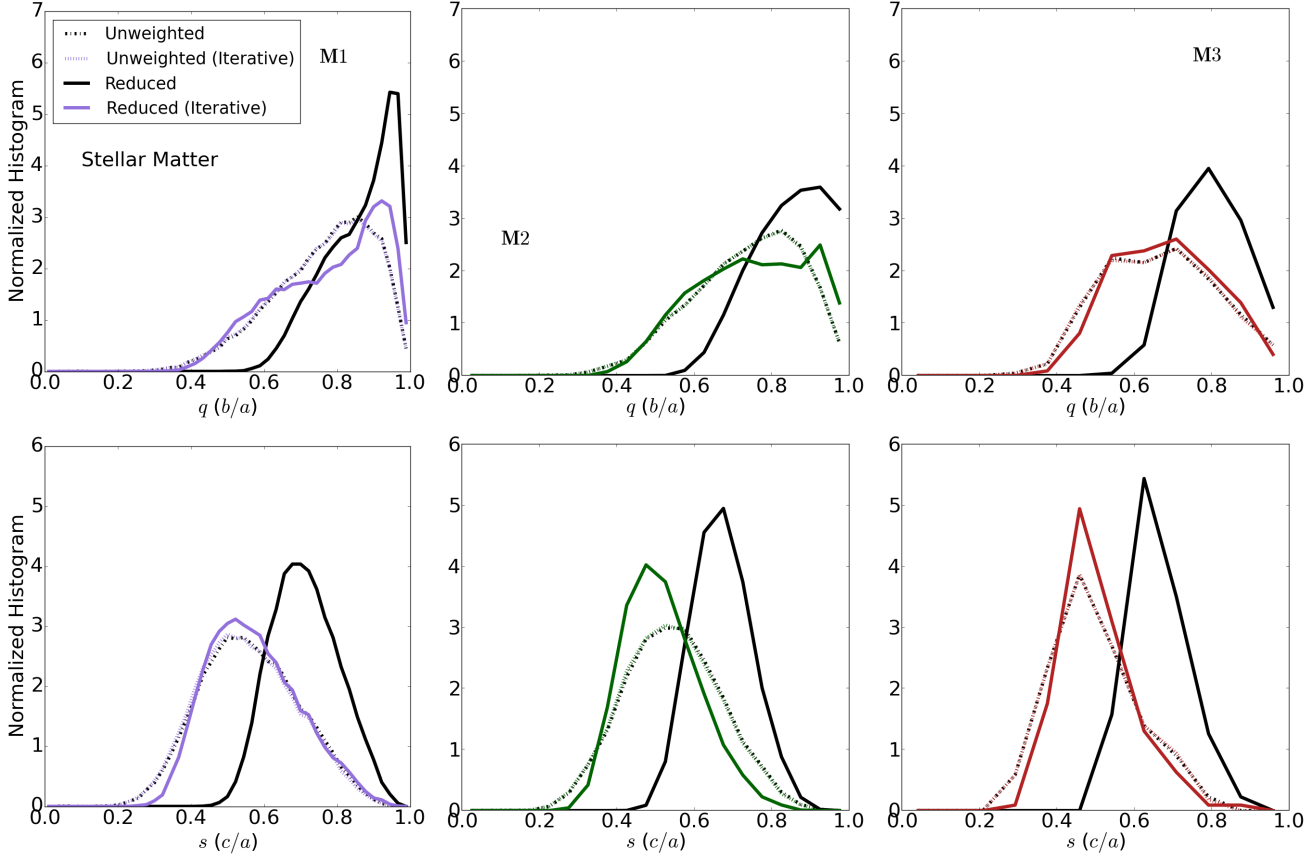


**Figure 2.** Normalized histograms of 3D axis ratios of stellar matter component in subhalos using different definitions of inertia tensor in mass bins M1, M2 and M3 at  $z = 0.3$ . *Top:*  $q (b/a)$ ; *Bottom:*  $s (c/a)$ .

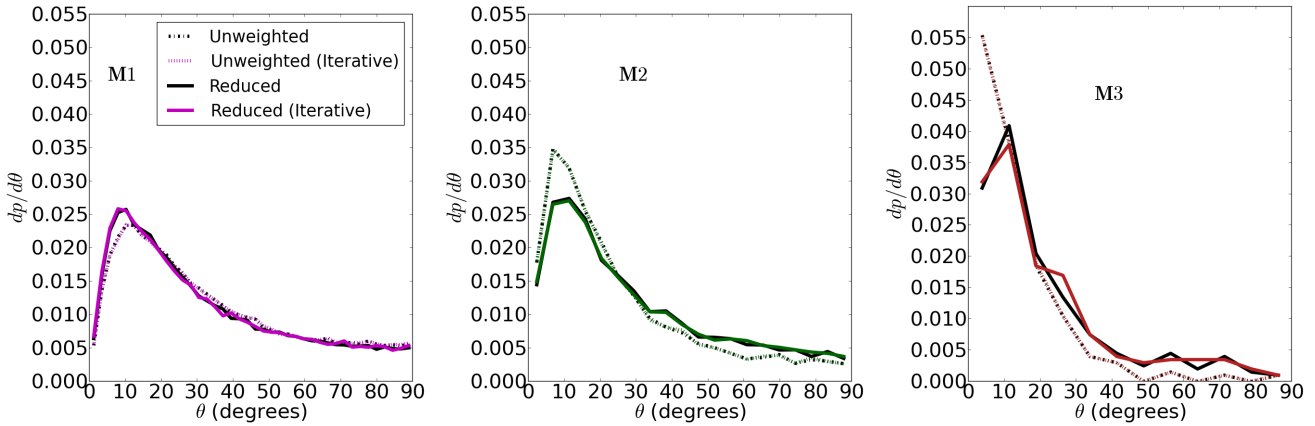


**Figure 3.** Normalized histograms of misalignment angles between the major axes of 3D shapes defined by the dark matter and stellar matter component in subhalos using different definitions of inertia tensor, in mass bins (M1, M2, and M3) at  $z = 0.3$ . Note that for uniformly distributed misalignment angles in 3D, the probability distribution is proportional to  $\sin \theta$ .

a significant change in the two point correlation functions, in comparison with the much stronger mass dependence of the two-point correlation shown in Sec. 6.1. So, we do not consider luminosity weighted inertia tensor in the rest of the sections in this paper.

## 5 COLOR DEPENDENCE OF INTRINSIC ALIGNMENTS

In this section, we investigate the color dependence of galaxy shape distributions, misalignment angle distributions, and two-point correlation functions. To do this, we roughly divide our entire sample of galaxies into red and blue types.



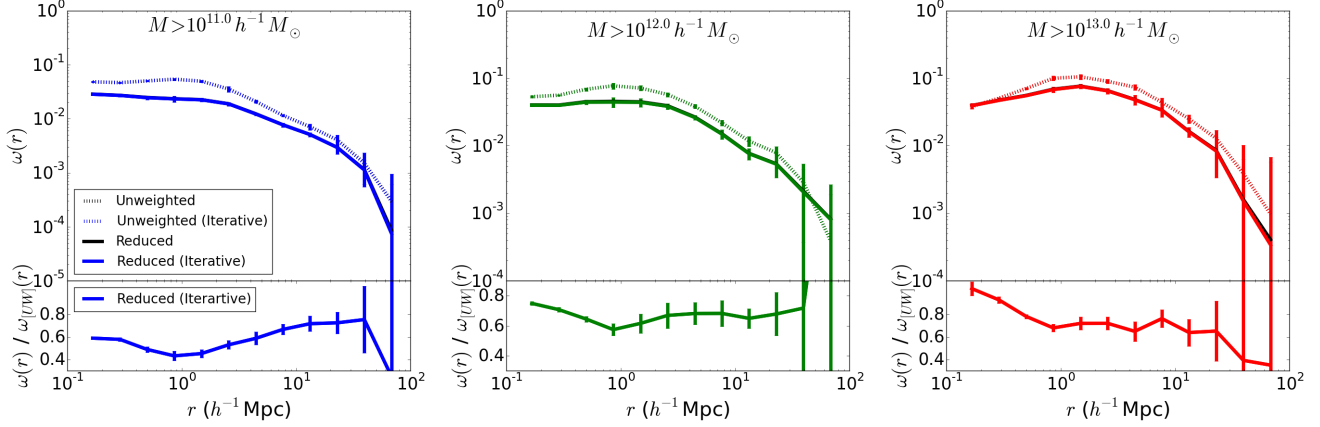


**Figure 4.** ED correlation function,  $\omega(r)$ , for the 3D shapes of stellar matter obtained using different definitions of inertia tensor in subhalos selected by a mass threshold. The *top* panel, shows the ED correlation function and the *bottom* panel shows the ratio of the signals obtained using iterative reduced inertia tensor with the unweighted inertia tensor. Note that in the *top* panel, the lines labeled Unweighted and Unweighted (Iterative); Reduced and Reduced (Iterative) are close enough that they cannot be easily distinguished. *Left:*  $M > 10^{11} h^{-1} M_{\odot}$  (24648 galaxies); *Middle:*  $M > 10^{12.0} h^{-1} M_{\odot}$  (2947 galaxies); *Right:*  $M > 10^{13.0} h^{-1} M_{\odot}$  (267 galaxies) at  $z = 0.3$ .

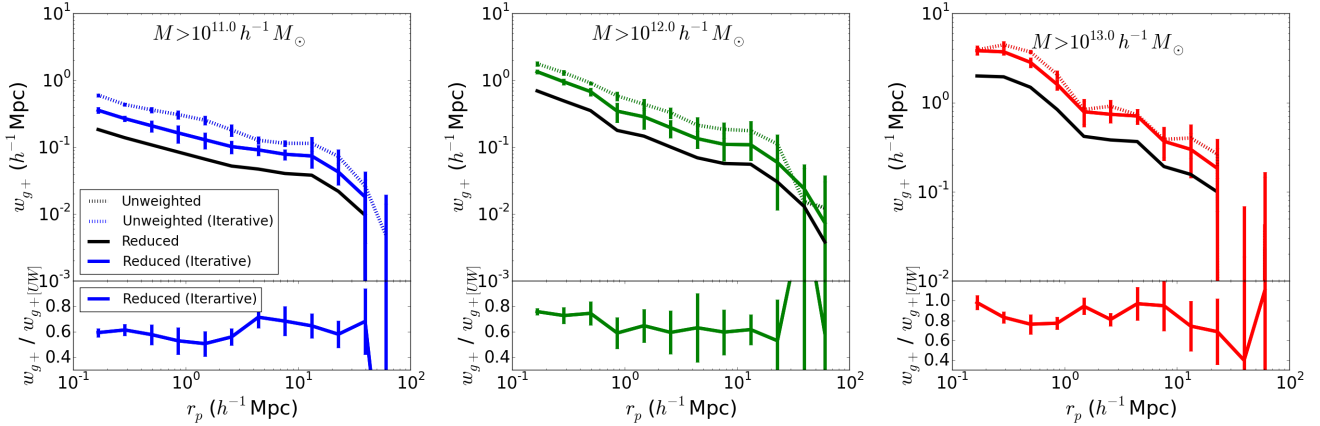


**Figure 5.**  $w_{g+}$  correlation function for the projected (2D) shapes of stellar matter obtained using different definitions of inertia tensor in subhalos selected by a mass threshold at  $z = 0.3$ . The *top* panel, shows the  $w_{g+}$  correlation function and the *bottom* panel shows the ratio of the signals obtained using iterative reduced inertia tensor with the unweighted inertia tensor. Note that in the *top* panel, the lines labeled Unweighted and Unweighted (Iterative) are close enough that they cannot be easily distinguished. *Left:*  $M > 10^{11} h^{-1} M_{\odot}$ ; *Middle:*  $M > 10^{12.0} h^{-1} M_{\odot}$ ; *Right:*  $M > 10^{13.0} h^{-1} M_{\odot}$ .

## 5.1 Division into blue and red galaxies

The color of a galaxy is obtained by calculating the difference in the absolute magnitudes in the SDSS  $u$ -band ( $M_u$ ) and  $r$ -band ( $M_r$ ) obtained from the simulation. In Fig. 8, we show a 2D histogram of color ( $M_u - M_r$ ) versus the stellar mass of subhalos at  $z = 0.3$ . Prior to plotting this histogram, we imposed a magnitude limit by eliminating galaxies with  $M_r < -18$  and eliminated galaxies with very bright AGNs.

Our colors do not exactly match those from observations, which have a clear bimodal distribution in the color-mass contour plot. So, we choose the median of  $M_u - M_r$  to roughly divide our sample of galaxies in the simulation into blue and red types. It is important to bear in mind that because of the procedure we have used, this might not be exactly analogous to the blue vs. red divisions used in studies of observed galaxies (e.g., Hirata et al. 2007). Together with the fact that color and morphology are not perfectly

correlated, this implies that our color based division is not same as a division into bulge-dominated and disk-dominated galaxies.

Codis et al. (2014) used a similar definition. They used the  $u - r$  rest-frame colors to divide their sample of galaxies in the simulation into three equal bins consisting of blue, red/blue and red types. Vogelsberger et al. (2014) divided the sample of galaxies in the Illustris simulation using the  $u - i$  color into blue, green and red types based on a star formation rate threshold, but they only produce a slightly bimodal distribution in colors that is not comparable with observations.

Here, we only consider the shapes obtained from the iterative reduced inertia tensor for our analysis in this section. We obtain similar results using the unweighted inertia tensor.

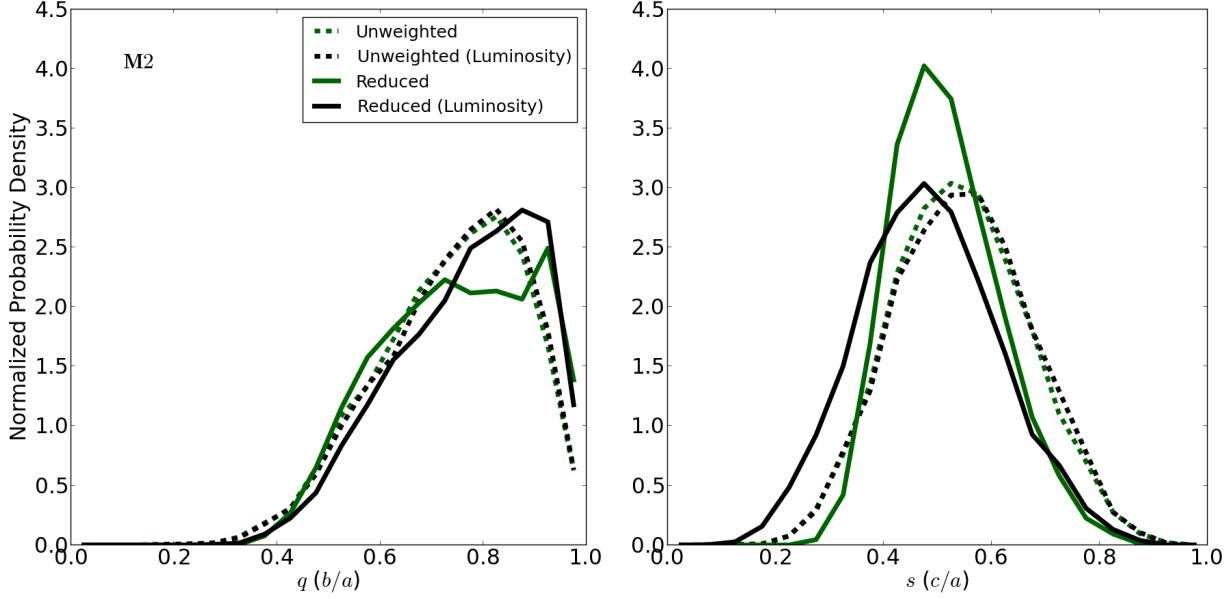


**Figure 6.** Normalized histograms of 3D axis ratios of stellar matter in subhalos using iterative unweighted and iterative reduced inertia tensors with each particle weighted by its luminosity or mass. Results are shown only for the mass bin M2. *Left:*  $q$  ( $b/a$ ); *Right:*  $s$  ( $c/a$ ).

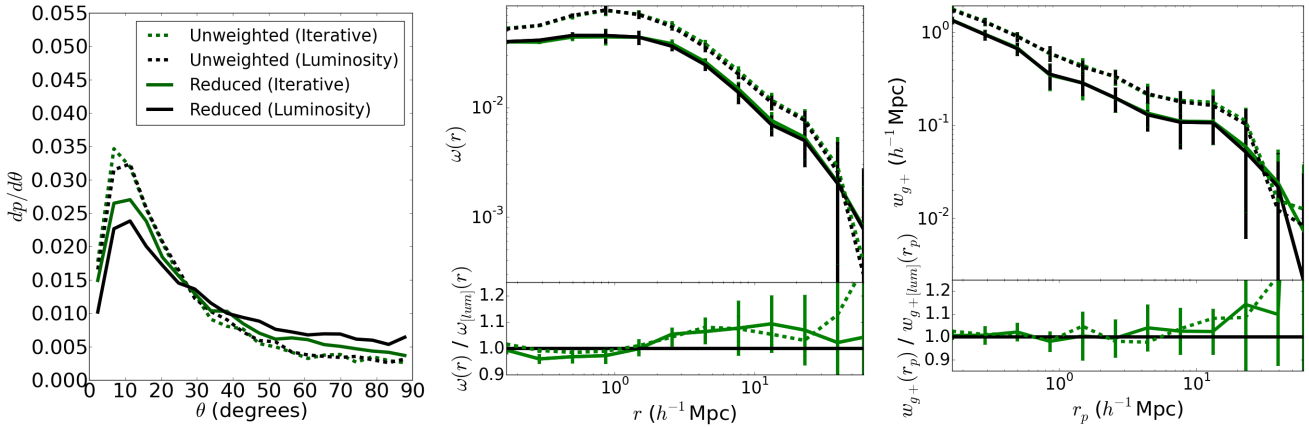


**Figure 7.** *Left:* Normalized histogram of misalignment angles using luminosity weighted shapes of stellar matter in subhalos in the mass bin, M2:  $10^{11.5} - 10^{13.0} h^{-1} M_{\odot}$  at  $z = 0.3$ . *Middle:* ED correlation of luminosity weighted shapes of stellar matter in subhalos for  $M > 10^{12} h^{-1} M_{\odot}$ . *Right:*  $w_{g+}$  correlation of luminosity weighted shapes of stellar matter in subhalos for  $M > 10^{12} h^{-1} M_{\odot}$ . For a direct comparison, the ratio of signals obtained using the mass and luminosity weighted inertia tensors are shown in the *bottom* panels.

## 5.2 Axis ratio distributions

The histograms of axis ratios of dark matter and stellar matter component in subhalos for the red and blue galaxies are shown in Fig. 9. The plots show that the red galaxies have slightly higher (rounder) axis ratios for the shapes defined by dark matter. For the shapes defined by stellar matter, the blue galaxies have slightly higher values of  $q$  ( $b/a$ ) and lower values of  $s$  ( $c/a$ ), indicating more oblate or disk-like shapes, as we would expect.

## 5.3 Misalignment angles and two-point correlation functions

The histogram of misalignment angles shown in the left panel of Fig. 10 indicates a larger misalignment between

dark matter halo and galaxy shapes in blue galaxies. The mean misalignment angles are  $29^{\circ} \pm 0.3^{\circ}$  and  $33^{\circ} \pm 0.3^{\circ}$  respectively for red and blue galaxies. If we wish to interpret these differences, we have to consider other factors that might change the distribution of misalignment angles, the most important of which is the mass. The mean masses of the sample of red and blue galaxies are similar. The red (blue) sample has a mean subhalo mass of  $8.0$  ( $7.9$ )  $\times 10^{11} h^{-1} M_{\odot}$ . Given the nearly consistent masses, the larger alignment for the red sample is not entirely due to mass.

In the middle panel of Fig. 10 we show the ED correlation for red and blue galaxies. The  $w_{g+}$  signals are plotted in the right panel. From the ratio plots of the intrinsic alignment signals for red and blue galaxies shown in the bottom

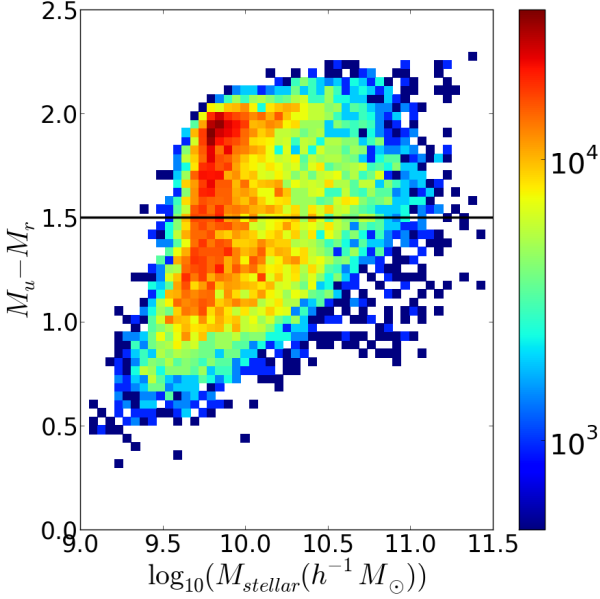


**Figure 8.** Rest-frame color ( $M_u - M_r$ ) versus stellar mass for galaxies in the simulation at  $z = 0.3$ .

panel, we conclude that there is no significant difference for our sample of red and blue galaxies.

## 6 MASS AND REDSHIFT DEPENDENCE OF TWO-POINT CORRELATION FUNCTIONS

In this section, we show the results for intrinsic alignment two-point correlation functions for shapes defined by the stellar matter component in subhalos. We focus in particular on the mass dependence and redshift evolution of the ED and  $w_{g+}$  correlation function.

### 6.1 Mass dependence

In Fig. 11, we consider the mass dependence of two-point correlation functions for shapes defined by stellar matter in subhalos. The left panel shows the ED correlation function for shapes obtained using iterative reduced inertia tensors. The galaxy samples here are selected based on total subhalo mass in the mass bins,  $M : 10^{11-12}h^{-1}M_\odot$ ,  $10^{12-13}h^{-1}M_\odot$  and  $10^{13-15}h^{-1}M_\odot$ . We observe a substantial increase in the amplitude of these correlation functions with increasing mass for both ED and  $w_{g+}$ . For  $M : 10^{13-15}h^{-1}M_\odot$ , the correlation function dips at small scales, possibly indicating a slightly random alignment of satellite subhalos with the orientation of the central galaxy. In a previous study, Lee et al. (2008) investigated the ED correlation functions from  $N$ -body simulations for shapes defined by dark matter. However, we know that the shape defined by stellar matter in galaxies is misaligned with the shape of host dark matter subhalo (Tenneti et al. 2014). This can significantly change the ED correlation function of shapes obtained with stellar matter when compared with results from an  $N$ -body simulations. For instance, previous studies have noted that there is a suppression in the intrinsic alignment signal due to misalignment of galaxy shape with the host dark matter shape

(Heymans et al. 2006; Okumura et al. 2009; Blazek et al. 2011). Qualitatively similar to our results of ED correlation using shapes of stellar matter component, Lee et al. (2008) also found that the correlation of dark matter shapes with the density field increases with halo mass at all scales. However, Lee et al. (2008) only measure the signal starting at  $r > 1h^{-1}\text{Mpc}$ . So, we cannot directly compare our results at small scales for the mass bin,  $M : 10^{13-15}h^{-1}M_\odot$ , where we observe a dip in the correlation.

In the right panel of Fig. 11, we considered the mass dependence in  $w_{g+}$  using the same mass bins. For this correlation function, the different ellipticities and orientation of shapes defined by stellar matter in galaxies can lead to a different correlation function, when compared with that obtained using dark matter shapes. For  $w_{g+}$ , we observe an increase in the amplitude of correlations with increasing subhalo mass threshold. The increase in intrinsic ellipticity-density correlation signal with halo mass is also predicted from  $N$ -body simulations (Heymans et al. 2006) and semi-analytic models (Joachimi et al. 2013). Unlike the ED correlation in 3D, and consistent with observations of  $w_{g+}$  for real galaxies (e.g., Hirata et al. 2007), we do not observe a dip in  $w_{g+}$  for  $M > 10^{13}h^{-1}M_\odot$  at small scales.

Although we do not show the mass dependence of intrinsic alignments for the shapes obtained using the iterative unweighted inertia tensor, it can be inferred from the plots shown in 4 and 5 that ED and  $w_{g+}$  correlation functions have similar mass dependence using the unweighted tensor. However, for comparison with observations, we expect that the iterative reduced inertia tensor might be a better choice as it gives more weight to the particles in the inner regions of subhalos. Hence, in the rest of this paper, we only present the two-point statistics using shapes obtained from the iterative reduced inertia tensor.

#### 6.1.1 Comparison of $w_{g+}$ and $w_{\delta+}$

The projected correlation function,  $w_{g+}$ , includes a factor of the galaxy bias due to the correlation with galaxy positions. In observational data, it is necessary to estimate a large-scale galaxy bias and use the linear bias approximation to remove this galaxy bias dependency, an approach which should fail on small to intermediate scales. In order to take the effect of subhalo bias at large scales into consideration, here we considered the ratio of two-point correlation functions using the dark matter particles to trace the density field with those obtained by using the subhalos to trace the density field. In the left panel of Fig. 12, we plotted the  $\omega_\delta(r)/\omega(r)$  correlation function at  $z = 0.3$  for shapes defined by stellar matter in galaxies, for  $M > 10^{11}h^{-1}M_\odot$ ,  $M > 10^{12}h^{-1}M_\odot$ , and  $M > 10^{13}h^{-1}M_\odot$  using the reduced iterative inertia tensor to calculate shapes. At small scales, we observe that the  $\omega_\delta(r)$  is a factor of 1.6–2 larger than  $\omega(r)$ , and the ratio is larger at higher mass thresholds. This result indicates that the shapes of massive galaxies are better aligned with the shape of the dark matter field than with the positions of other galaxies. The right panel shows a similar plot for the projected shape correlation function ( $w_{\delta+}$ ). Again, we observe a larger  $w_{\delta+}$  at small scales, and the ratio increases with mass threshold. In both the plots, the ratio is nearly constant at large scales for all mass thresholds, and is inversely proportional to the large-scale bias of the den-

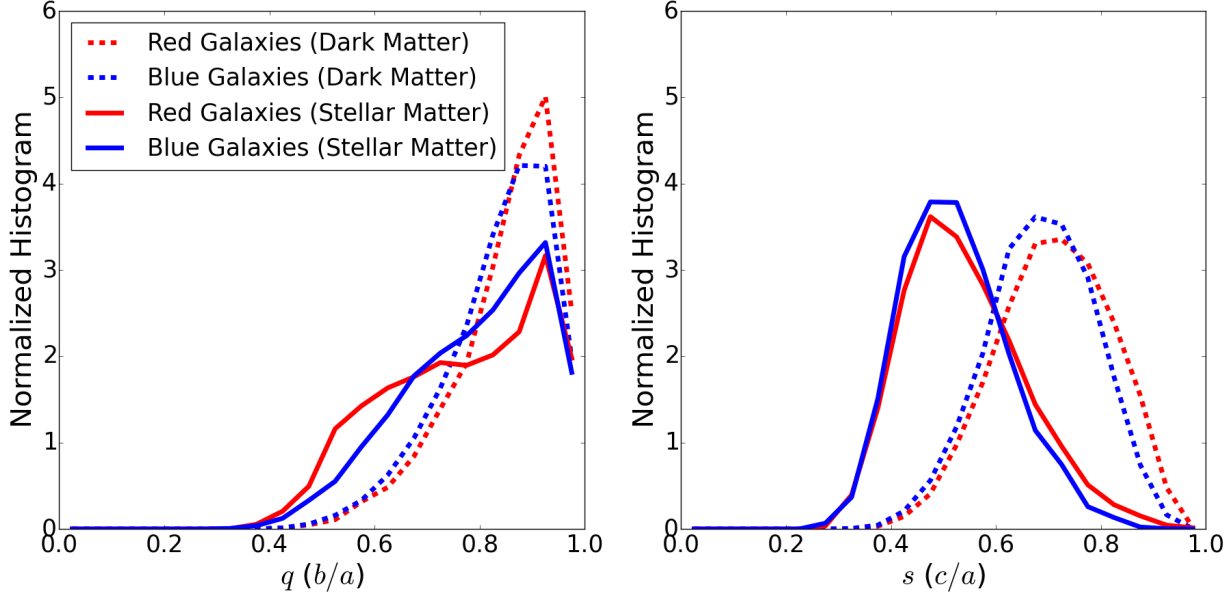


**Figure 9.** Normalized histograms of axis ratios ( $q$ ,  $s$ ) of dark matter and stellar matter component in subhalos for blue (6343 galaxies) and red (6343 galaxies) galaxies at  $z = 0.3$ . *Left:*  $q$  ( $b/a$ ); *Right:*  $s$  ( $c/a$ ).

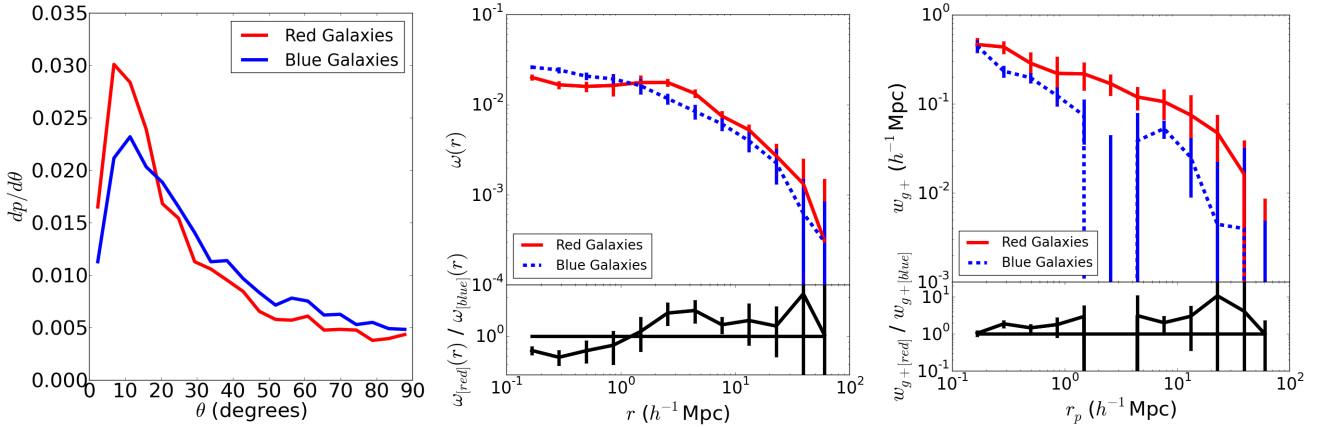


**Figure 10.** Comparison of misalignment angles and two-point correlation function in red and blue galaxies at  $z = 0.3$ . *Left:* Histogram of misalignment angles; *Middle* ED position angle statistic; *Right*  $w_{g+}$  projected shape correlation function. At around  $\sim 1h^{-1}\text{Mpc}$ , the correlation function becomes negative for the blue galaxies.

sity tracer sample (all subhalos in the simulation). Since the simulation includes relatively low mass subhalos, their average bias is  $< 1$  and hence the ratio that is plotted is slightly above 1.

## 6.2 Redshift evolution

We show the redshift evolution of intrinsic alignment two-point correlation functions by plotting the ratios of ED and  $w_{g+}$  at  $z = 1.0$ ,  $0.3$ , and  $0.06$  to the corresponding quantities at  $z = 0.3$  for  $M > 10^{11}h^{-1}M_{\odot}$ . In the left (right) panel of Fig. 13, we show this ratio for the ED ( $w_{g+}$ ) correlation functions with three subhalo mass threshold values. We observe that (for fixed mass threshold) the amplitude of the ED correlation function decreases significantly at all scales and for all mass thresholds as we go to lower redshifts. Us-

ing  $N$ -body simulations, Lee et al. (2008) also found that the amplitude of the ED correlation function decreases at lower redshifts. However, the  $w_{g+}$  correlation function does not exhibit a strong dependence on redshift. This is due to a difference in the shape distributions that compensates for the redshift evolution of position angle alignments shown by the results for  $\omega$ .

The linear alignment model predicts that for the range of redshifts considered here,  $w_{\delta+}$  varies roughly as  $(1+z)^{-0.7}$  (Hirata et al. 2007). We do not detect any significant redshift evolution of  $w_{\delta+}$  for most of our samples. However, this particular test for redshift evolution based on mass (or luminosity) threshold samples may not be fair for intrinsic alignments evolution, since we are not comparing results for a high-redshift sample of progenitors of the low-redshift sample at a given mass threshold (due to additional mergers

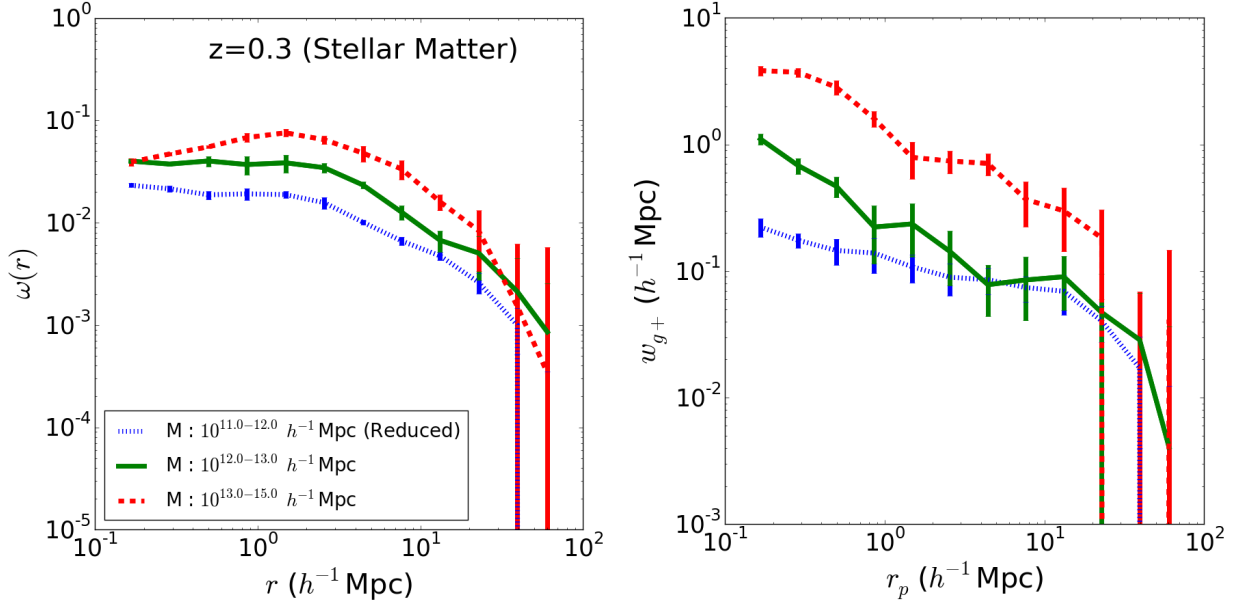


**Figure 11.** Mass dependence of two-point correlation functions for shapes defined by stellar matter in subhalos at  $z = 0.3$  using iterative reduced inertia shape tensors. *Left:* Position angle statistic, ED correlation function; *Right:* Projected shape-correlation function,  $w_{g+}$ .

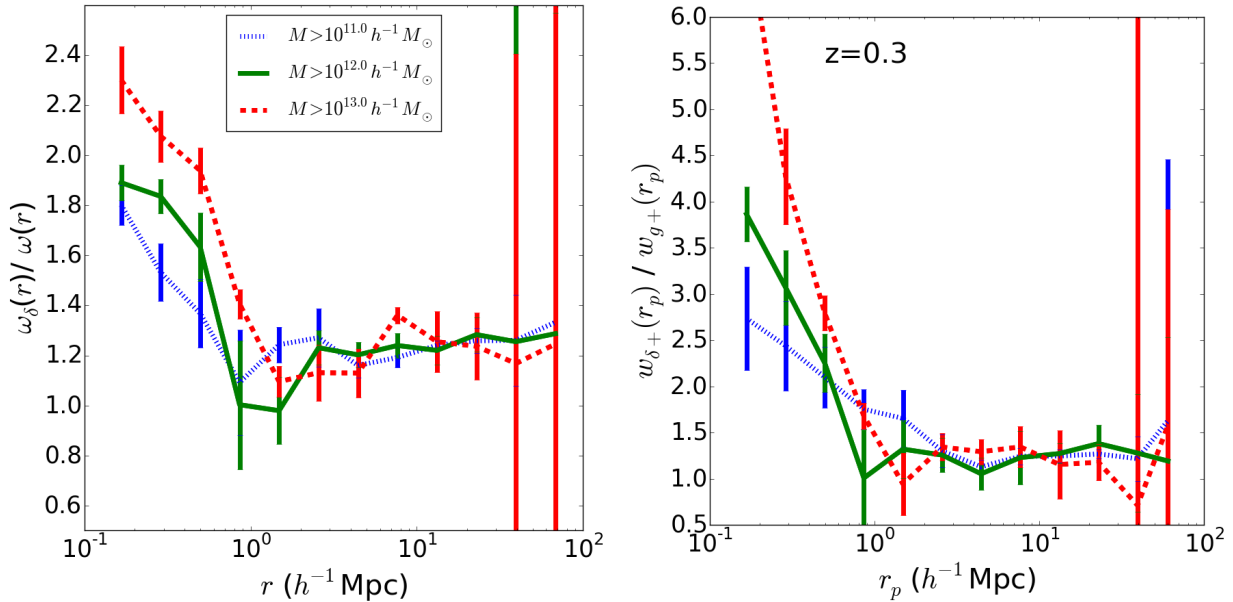


**Figure 12.** *Left:* Ratio of  $\omega_{\delta}(r)$  (density field traced by dark matter particles) to  $\omega(r)$  *Right:* Ratio of  $w_{\delta+}(r_p)$  correlation function, where the density field is traced by dark matter particles, to  $w_{g+}(r_p)$  (density field traced by subhalos).

and mass accretion). We defer the exploration of this effect to future work.

## 7 TWO POINT CORRELATION FUNCTIONS: CENTRALS AND SATELLITES

A central subhalo is located at or near the potential minimum of its host halo. The remaining subhalos of that host halo are satellites. Here, we investigate the intrinsic alignment two-point correlation functions for central and satellite

subhalos separately, by looking at the projected shape correlation in various mass bins.

### 7.1 Alignments of central and satellite galaxies

Observationally, the distribution of satellites around central galaxies has been found to be anisotropic, with more satellites along the major axis of the central galaxy (e.g., Sales & Lambas 2004; Brainerd 2005; Yang et al. 2006; Nierenberg et al. 2012; Li et al. 2013; Wang et al. 2014; Lee et al. 2014). This has also been studied through  $N$ -body simula-

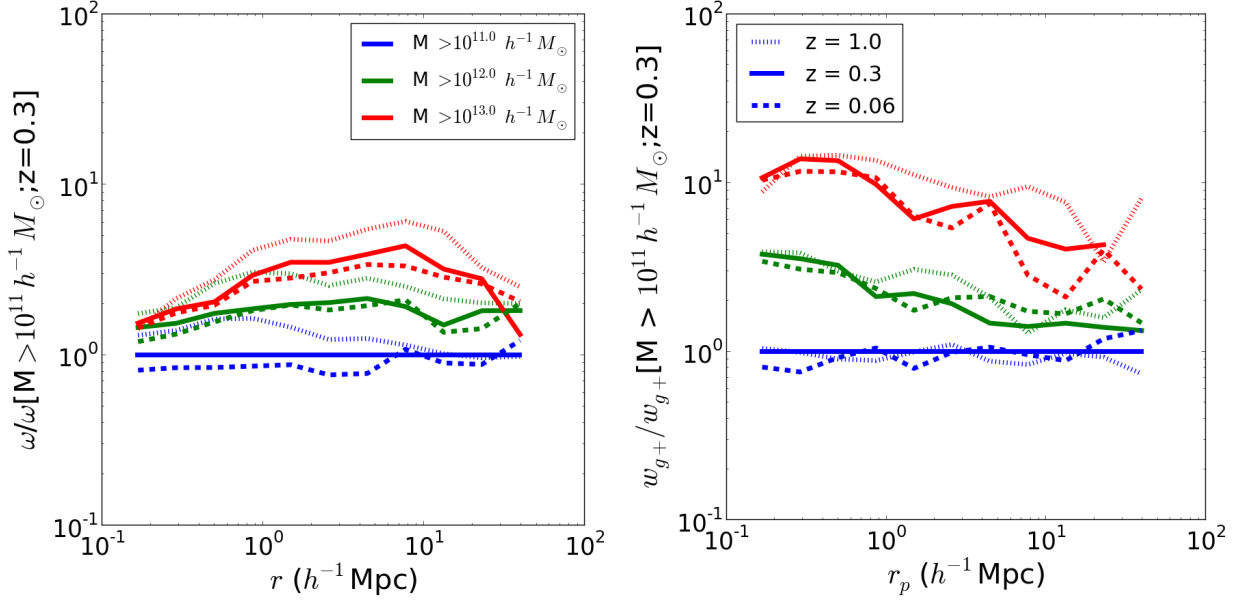


**Figure 13.** Ratio plot of two-point correlation functions at redshifts  $z = 1.0, 0.3$  and  $0.06$  and various mass thresholds to the corresponding value at  $z = 0.3$  for  $M > 10^{11.0} h^{-1} M_{\odot}$ . *Left:* ED; *Right:*  $w_{g+}$ .

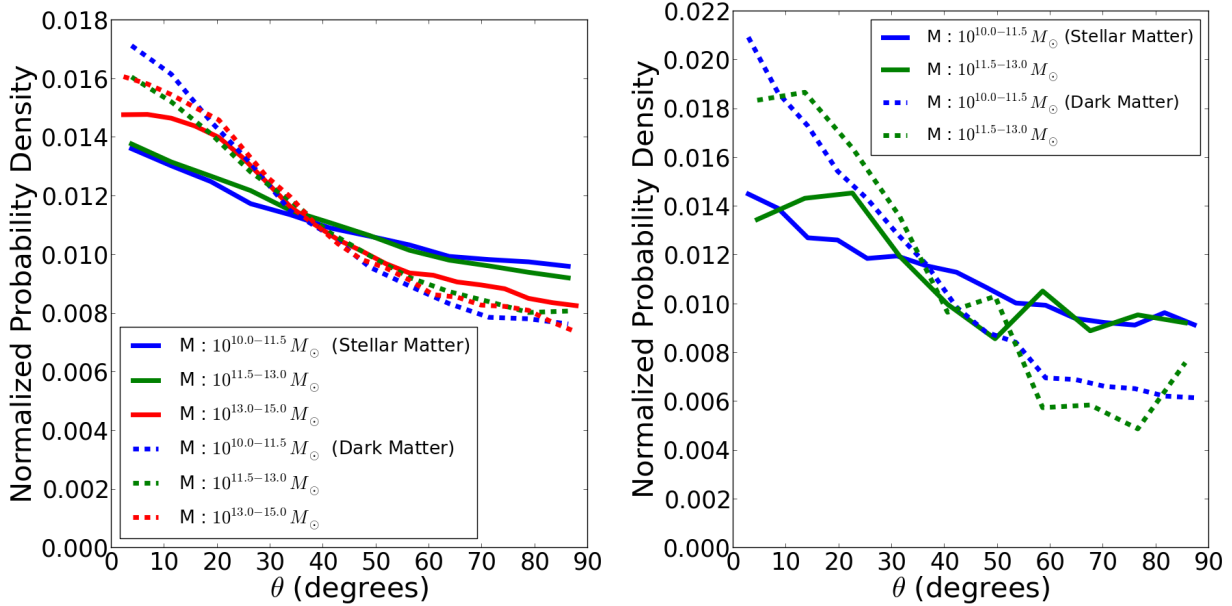


**Figure 14.** *Left:* Normalized histogram of alignment angle of the major axis of the 2D stellar shape of a central galaxy with satellite subhalos in mass bins,  $M1, M2$  and  $M3$  of central subhalo mass at  $z = 0.3$ . *Right:* Normalized histogram of alignment angles of the major axis of the 2D stellar shape of satellite galaxies with host halo in mass bins,  $M1$  and  $M2$  of satellite subhalo mass at  $z = 0.3$ .

tions (Faltenbacher et al. 2008; Agustsson & Brainerd 2010; Wang et al. 2014) and hydrodynamic simulations of smaller volume (Libeskind et al. 2007; Deason et al. 2011). However,  $N$ -body simulations overestimate the strength of the alignment signal if it is assumed that the shape of central galaxy follows the shape of dark matter halo (Kang et al. 2007; Agustsson & Brainerd 2010). In a recent paper, Dong et al. (2014) used a large volume hydrodynamical simulation without AGN feedback to study this problem.

Here, we explore the distribution of the location of satel-

lite subhalos with respect to the major axis of the central subhalo in the host halo. The left panel of Fig. 14 shows the histogram of angle between the major axis of shapes of dark matter and stellar matter of a central subhalo with the line joining the satellite subhalos. From the plot, we can conclude that the satellite subhalos are more concentrated along the major axis of its central galaxy. Our results are qualitatively consistent with results from  $N$ -body simulations by Faltenbacher et al. (2008); Wang et al. (2014). Using hydrodynamic simulations of smaller volume, Deason et al.

(2011) found that the satellites are more distributed along the axis of the shape determined by dark matter component of a central subhalo, when compared with that of stellar matter. We also confirm this finding with a large statistical sample. From the plot, we can observe that there is no significant mass dependence in the distribution of satellites along the major axis of the subhalo with shape determined using dark matter particles. On the other hand, for shapes defined by stellar matter of galaxies, we observe that the alignment increases with increasing subhalo mass with the mean alignment angles being  $42.0^\circ$ ,  $41.5^\circ$  and  $39.6^\circ$  in the mass bins,  $M1$ ,  $M2$  and  $M3$  respectively. This is due to a greater misalignment angle between the shapes defined by the dark matter and stellar matter in less massive central galaxies. Dong et al. (2014) also studied the spatial distribution of satellite galaxies with respect to the orientation of their host central galaxy using a large volume hydrodynamical simulation. They found more alignment in massive halos with mean alignment angles varying from  $45^\circ - 40^\circ$  in the mass range,  $10^{11} - 10^{14} h^{-1} M_\odot$  which agrees qualitatively with our findings.

We also investigate the orientation of satellite galaxies with respect to the location of its central subhalo. The right panel of Fig. 14 shows the alignment of the major axis of the shapes of satellite galaxies with the direction to their central subhalo. This is the radial alignment signal, which has been studied for dark matter component of satellites using  $N$ -body simulations (Kuhlen et al. 2007; Pereira et al. 2008; Faltenbacher et al. 2008) and hydrodynamic simulations (Knebe et al. 2010). These studies found that the orientation of satellite subhalos is not random, but point more towards the center of their host halo. Here, we observe that the shapes of stellar matter in satellites are also more aligned with the direction to their host halo. Recent observational measurements of Schneider et al. (2013); Sifón et al. (2014) have not detected radial alignment of satellite galaxies with their host halo.

## 7.2 $w_{g+}$ and $w_{\delta+}$ for centrals and satellites

In Fig. 15, we show the  $w_{g+}$  and  $w_{\delta+}$  correlation function for centrals and satellites in mass bins,  $M1$  and  $M2$ . In the highest mass bin,  $M3$ , the signal for satellites is not shown due to lack of sufficient number of satellite subhalos. The figure shows that at small scales, the  $w_{g+}$  and  $w_{\delta+}$  signal for satellites is larger than that for centrals for subhalos in the mass bin  $M1$ . This is interesting and could be due to following possibilities: 1. Satellite subhalos have stronger alignments with the local tidal fields than the central subhalos. Note that within a halo, tidal fields are predominantly radial, consistent with the radial alignments of satellites. More generally, since central subhalos are in reality the innermost subhalo, this could imply some radial dependence of intrinsic alignments. 2. Another possibility is that satellite and central intrinsic alignments are not very different, but the overall intrinsic alignments signal depends on the host halo mass. In this case, more massive halos with more satellite subhalos will get higher weight in satellite correlations but not in central correlations. This could also push up the  $w_{g+}$  and  $w_{\delta+}$  signal for satellites. We speculate that final result is likely to be combination of these two effects, with radial dependence being the more dominant factor. In

mass bin  $M2$ , the plot shows that there is no statistically significant differences in the intrinsic alignments of centrals and satellites at any scale.

At large scale, it is expected that the intrinsic alignment signal due to satellites goes to zero in the halo model (Schneider & Bridle 2010), based on the assumption that the satellite subhalos are uniformly distributed throughout the host halo pointing towards the center. However, the latter assumption is not quite true in reality. As shown in Sec. 7.1, the satellite subhalos have a tendency to be distributed more along the major axis of the central galaxy and are also radially aligned. Hence, they “inherit” the large-scale intrinsic alignments of the host halo at some level. This could be the explanation for the fact that the satellite  $w_{g+}$ , while dropping on large scales, is still non-zero.

From Fig. 15, we can also see that as we go to higher masses, the amplitude of intrinsic alignments in central subhalos increases.

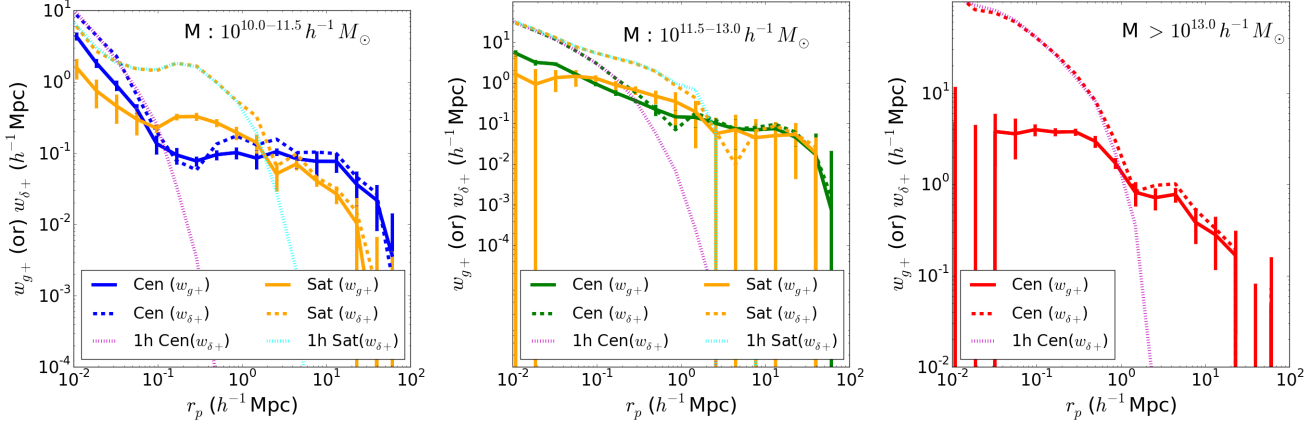
In addition, the transverse separation,  $r_p$ , where we observe a slight dip or change in the shape of the correlation function shifts to smaller values as we go to lower masses of central subhalos. This change of shape indicates a region of transition from the 1-halo term at small scales to the 2-halo term at large scales. To further illustrate our point, we also show the 1-halo term of  $w_{\delta+}$  for central and satellite subhalos in these mass bins. This is directly calculated by correlating the shape of a galaxy with the location of dark matter particles that belong to its host halo. As seen from the plot, the 1-halo term follows the shape of  $w_{\delta+}$  at small scales and drops to zero at large distances (on scales comparable to the virial radius), where the 2-halo term is becoming more significant.

## 8 MODELING, COMPARISONS AND PREDICTIONS

In this section, we present the results of fitting the non-linear alignment (NLA) model to the MB-II intrinsic alignment two-point correlation functions. The NLA model has been shown to describe realistic galaxy intrinsic alignments. Comparing the results from the simulation with the NLA model will help us understand on what scales the NLA model describes the alignments in MB-II. Additionally, these fits are a much more compact way to represent our predictions, encapsulating all the information about the scale-dependence of the signal as a single amplitude parameter and a well-known physical model. On small-scales, the NLA model does not describe the signals well, so we provide simple power-law fits for these scales. We also compare the intrinsic alignment two-point correlation functions in MB-II with those in real data. There are two purposes of this comparison. The first is simply to confirm that MB-II gives physically-reasonable results for samples for which intrinsic alignments have been robustly detected. The second is to then make predictions for samples that will be used for lensing by upcoming surveys.

### 8.1 Fitting models to MB-II correlation functions

Here we present results of fitting NLA and power law functions to our predictions for  $w_{g+}$  and  $w_{\delta+}$  from MB-II.



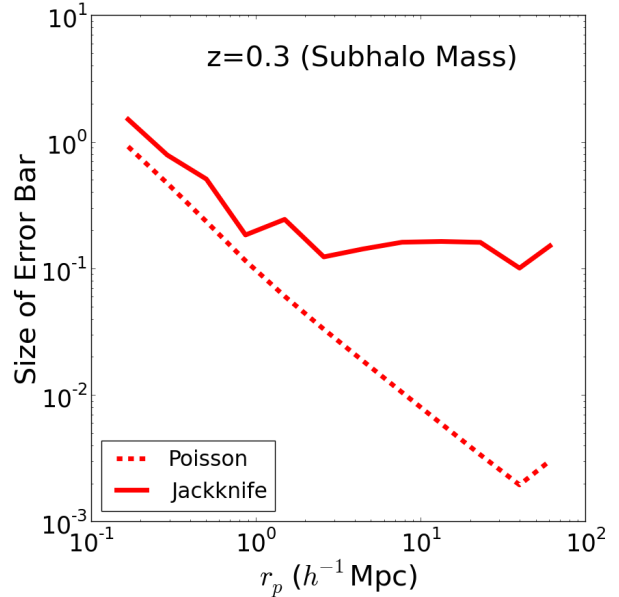
**Figure 15.**  $w_{g+}$  and  $w_{\delta+}$  correlation function for centrals and satellites at  $z = 0.3$ . *Left:* M1:  $10^{10-11.5} h^{-1} M_{\odot}$ ; *Middle:* M2:  $10^{11.5-13.0} h^{-1} M_{\odot}$ ; *Right:* M3:  $> 10^{13.0} h^{-1} M_{\odot}$ . The labels “Cen” and “Sat” refer to the correlation functions ( $w_{g+}$ ,  $w_{\delta+}$ ) of centrals and satellites respectively. Similarly, “1h Cen” and “1h Sat” refer to the 1-halo term of  $w_{\delta+}$  for central and satellite subhalos respectively. The number of central galaxies is 23014, 7415 and 255 in mass bins M1, M2 and M3 respectively.

Fig. 17 shows an example of models fitted to the measurements for two different samples defined by luminosity bins,  $M_r \leq -22.6$  and  $M_r \in [-22.6, -20.3]$ . More examples and tables with fit parameters can be found in Appendix A. We fit the NLA model in the range  $6 < r_p < 25 h^{-1} \text{Mpc}$ . Beyond  $25 h^{-1} \text{Mpc}$ , the MB-II predictions are dominated by cosmic variance. We fit  $w_{g+}$  and  $w_{\delta+}$  simultaneously assuming the same  $A_I$  for both, and an additional large-scale (constant) subhalo bias  $b_D$  for  $w_{g+}$ . As can be seen in Fig. 17, the NLA model fits the data well in the fitting range and can be extended down to  $r_p \sim 4 h^{-1} \text{Mpc}$ , below which the signal differs in both amplitude and scale dependence. We add a note of caution that we use the simple weighted least squares method to fit the model using only the diagonal terms in the covariance matrix, which underestimates the errors on the parameters when compared with the errors on data points. The errors shown on data points are calculated from jackknife variance, but due to the limited size of our simulation box, the jackknife errors on the maximum scales used are not very reliable. Fig. 16 shows a comparison of jackknife and Poisson error bars. The Poisson errors tend to be very small (and are certainly underestimated above a few  $h^{-1} \text{Mpc}$  scales, where cosmic variance will be important). However they are within a factor of 1.5–2 of the jackknife errors on small scales, which is reasonable. While Poisson errors are underestimated, the scale dependence of jackknife errors suggest that they are cosmic variance dominated and due to the limited size of the simulation box, the covariance matrix is very noisy. Keeping in mind the limitations of our jackknife covariance matrix, we do not attempt a more sophisticated fitting method to get better error estimates on the model parameters.

On small scales, we fit a power law function separately to  $w_{g+}$  and  $w_{\delta+}$ , in the range  $0.1 < r_p < 1 h^{-1} \text{Mpc}$ . The power law function is of the form:

$$w_{g+} = P_A r_p^{P_I} \quad (18)$$

Fig. 18 shows intrinsic alignments amplitudes for  $w_{g+}$  as function of average luminosity and redshift of the sample, for different samples defined with different luminosity bins.



**Figure 16.** Comparison of the size of Poisson and jackknife error bars in the calculation of  $w_{g+}(r)$  for subhalo mass-selected samples.

We see clear evolution with luminosity and mild evolution with redshift. More luminous objects show stronger intrinsic alignments, qualitatively consistent with LRG observations. Within the NLA model, where it is assumed that intrinsic alignments are set at time of galaxy formation, we do not expect any redshift evolution of  $A_I$ . This is consistent with LRG observations, where no significant redshift dependence for  $A_I$  is detected (Joachimi et al. 2011b), admittedly with a narrower redshift range than considered here. LRG are, however, a special population of old, very massive, passively evolving galaxies. Our sample in MB-II is much more diverse in properties and is heavily dominated by much less massive galaxies that will include a variety of formation and evolutionary histories, including recent mergers and accretion. This is expected to change the intrinsic alignments sig-



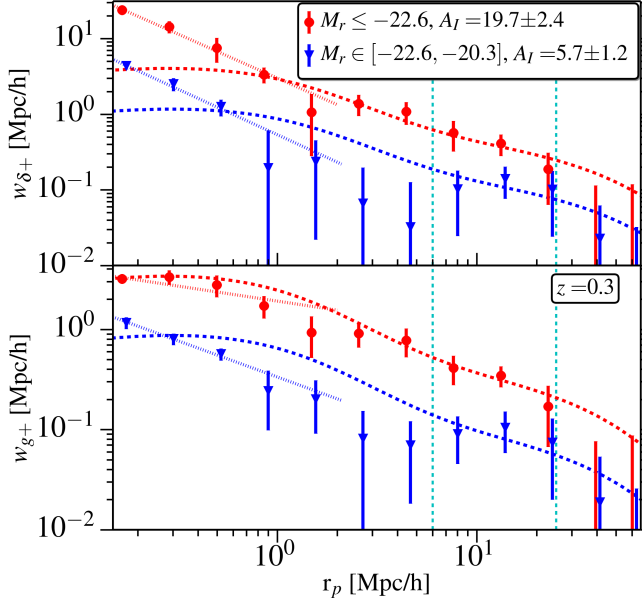


**Figure 17.** NLA and power law fitting to  $w_{\delta+}$  (top) and  $w_{g+}$  (bottom) for two different samples defined by luminosity bins. Vertical lines show the range over which we fit the NLA model ( $6h^{-1}\text{Mpc} < r_p < 25h^{-1}\text{Mpc}$ ). Note that the power law is fitted only for  $r_p < 1h^{-1}\text{Mpc}$ , though the function is shown out to  $r_p \sim 2h^{-1}\text{Mpc}$ .

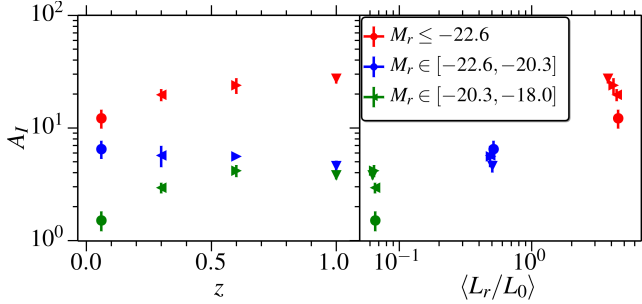


**Figure 18.** NLA amplitude,  $A_I$ , as a function of redshift for different luminosity samples. The horizontal axis indicates the average mass, luminosity or redshift of different samples. Points are colored by sample definition, while markers are set according to the redshift.

nal at all scales. We see clear redshift evolution in two of the three samples defined by luminosity bins, with the middle bin showing negligible evolution. For the brightest and faintest samples, we observe that the NLA model amplitude decreases at lower redshifts, which suggests that dynamical processes such as galactic mergers play some role in intrinsic alignments evolution at those luminosities.

To quantify the evolution of intrinsic alignments with redshift, mass and luminosity, we fit the non-linear alignment model amplitude  $A_I$  with the following functions:

$$A_I = A \left( \frac{\langle L_r \rangle}{L_0} \right)^{\alpha_L} (1+z)^{\alpha_z} \quad (19)$$

**Table 1.** Results of fitting different parameters (luminosity bin samples only) to find their mass and luminosity evolution (Eq. 20 and 19). Different columns are the parameters that go into Eq. (20) and (19) while different rows are for different intrinsic alignments model parameters, with  $A_I$  being the NLA amplitude,  $P_A$  and  $P_I$  are power law fits (Eq. 18) to  $w_{g+}$  and  $P_A^\delta$  and  $P_I^\delta$  are power law fits to  $w_{\delta+}$ .

Parameter	$A$	$\alpha_L$	$\alpha_z$
$A_I$	$6.7 \pm 1.7$	$0.47 \pm 0.08$	$0.5 \pm 0.5$
$P_A$	$0.59 \pm 0.08$	$0.48 \pm 0.05$	$-0.7 \pm 0.2$
$P_I$	$-0.49 \pm 0.08$	$0.09 \pm 0.06$	$0.5 \pm 0.3$
$P_A^\delta$	$1.5 \pm 0.3$	$0.6 \pm 0.1$	$-1.7 \pm 0.5$
$P_I^\delta$	$-1.1 \pm 0.1$	$0.1 \pm 0.03$	$0.1 \pm 0.2$

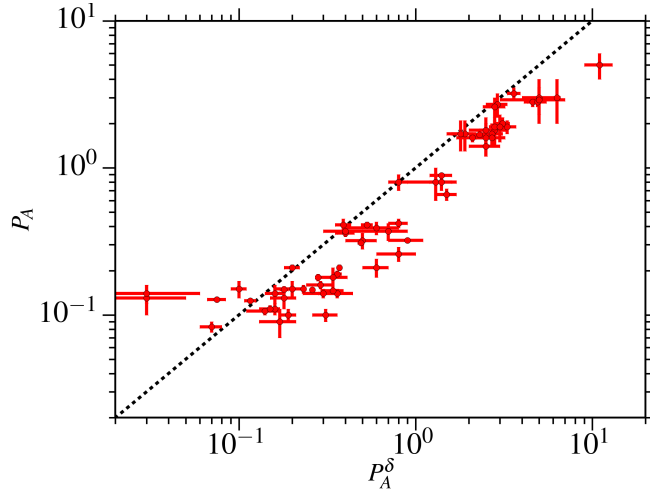


**Figure 19.** Comparison of power law amplitude for  $w_{g+}$  ( $P_A$ ) and  $w_{\delta+}$  ( $P_A^\delta$ ) for various samples used in this work. The dotted line shows the  $x = y$  relation.  $w_{\delta+}$  is observed to have systematically higher amplitude than  $w_{g+}$  for separations below  $1h^{-1}\text{Mpc}$ .

$\langle L \rangle$  is the average  $r$ -band luminosity, normalized by pivot luminosity  $L_0$  corresponding to  $r$ -band magnitude  $M_r = -22$ . Results from the fitting are shown in Table 1. We also show results from similar fitting to power law amplitude and index.

Doing a similar fit to  $A_I$  in luminosity and redshift to LRG samples, Joachimi et al. (2011b) got  $\alpha_L = 1.13^{+0.25}_{-0.20}$  and  $\alpha_z = -0.27^{+0.80}_{-0.79}$  (MegaZ-LRG + SDSS LRG + L4 + L3). Our power law indices are different, with our samples showing weaker luminosity evolution than LRGs. This is likely due to differences in the samples, since our samples do not include color cuts, and also extend to fainter luminosities. Our results are qualitatively consistent with results of Joachimi et al. (2013), who used semi-analytical approach to populate dark matter halos in Millennium simulation and measured the intrinsic alignments signal. When they measured intrinsic alignments amplitudes as a function of luminosity, they found a shallower luminosity dependence at the faint end than for LRGs. Our  $\alpha_z$  is consistent with zero within  $1\sigma$ , consistent with Joachimi et al. (2011b) and Joachimi et al. (2013).

Figs. 19 and 20 show the comparisons of power-law parameters (Eq. 18) fit to  $w_{\delta+}$  and  $w_{g+}$  for different samples

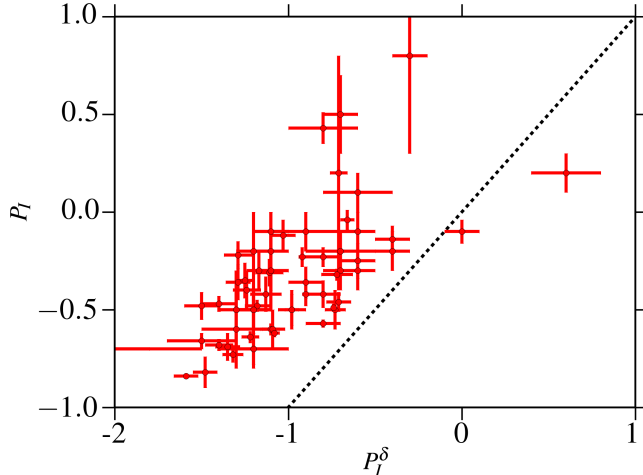


**Figure 20.** Comparison of power law index for  $w_{g+}$  ( $P_l$ ) and  $w_{\delta+}$  ( $P_l^\delta$ ) for various samples used in this work. The dotted line shows the  $x = y$  relation.  $w_{\delta+}$  has a systematically steeper slope than  $w_{g+}$  for separations below  $1 h^{-1} \text{Mpc}$ .

used in this work.  $w_{\delta+}$  has systematically higher amplitude and steeper power-law index than  $w_{g+}$ , which implies that  $w_{g+}$  is more flattened compared to  $w_{\delta+}$  below  $1 h^{-1} \text{Mpc}$ . The flattening of  $w_{g+}$  at small scales is likely due to the effects of non-linear bias of the subhalo sample used as density tracer. However, as observed in Fig. 12, the ratio of  $w_{\delta+}/w_{g+}$  changes for different mass threshold samples, which means that there could be some differences due to intrinsic alignments signal as well. Subhalos are biased tracers of density field and it is conceivable that intrinsic alignments signal at small scales can change when subhalos are used as the density tracers (for example, there may not be enough subhalos around a galaxy at small scales to fairly measure the intrinsic alignments signal). This can have important implications for observational studies of intrinsic alignments, where we can only use galaxies as biased tracers of the density field, so the small scale intrinsic alignments could be underestimated.

## 8.2 Comparison with luminous galaxy intrinsic alignments

In Fig. 21, we show the  $w_{g+}$  correlation function for the subhalos selected by luminosity in  $r$ -band such that the absolute AB magnitudes satisfy  $M_r \leq -22.6$ . The error bars shown here are obtained using the jackknife technique. The observational measurements are obtained from an SDSS LRG sample in the redshift range  $0.27 < z < 0.35$ , with luminosity cuts as defined in Hirata et al. (2007). The galaxies from the simulation are selected to match the luminosity threshold of the Bright LRG sample ( $M_r \leq -22.6$ ), against which we compare our results. The amplitude of the predicted  $w_{g+}$  for this sample is in good agreement with the observational results for the LRG sample<sup>5</sup>. The mass range of the galaxies from the simulation roughly corresponds to a subhalo

<sup>5</sup> The bias of the density sample in both simulations and observations has been taken into account in this comparison.

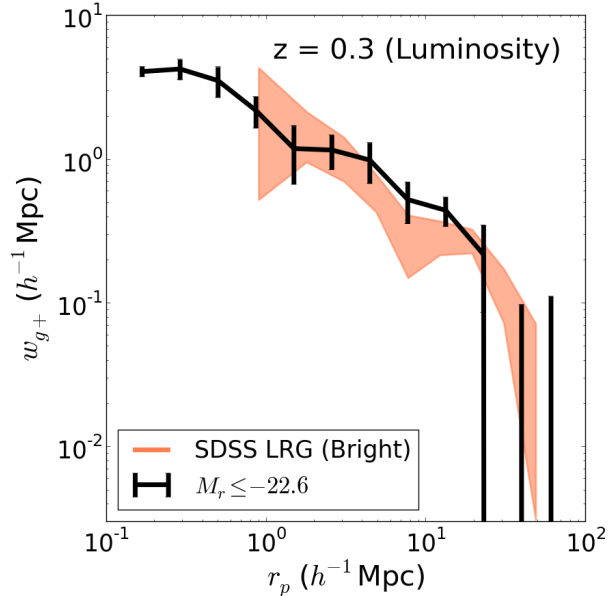


**Figure 21.**  $w_{g+}$  correlation function for galaxies selected according to  $r$ -band luminosity (such that  $M_r \leq -22.6$ ) and comparison with observational results using SDSS LRG sample. Note that the bias of the density tracer sample has been taken into account in order to make a fair comparison, by dividing  $w_{g+}$  with the large scale linear bias.

mass threshold of  $M > 10^{13} h^{-1} M_\odot$  which is indeed the appropriate halo mass range for LRGs. However, there is an important caveat in this comparison. The LRG sample has color cuts and so, unlike the simulated galaxies, the LRG samples are not perfectly luminosity selected. Hence, it is difficult to make an exact comparison of the the amplitude of correlation function in spite of selecting the same luminosity thresholds. If we ignore the amplitude, which is likely to be a nuisance parameter that gets marginalized over in a typical intrinsic alignment mitigation scheme, what is more important is that the scaling with transverse separation is consistent with that in real data, as is the scaling with mass that was shown earlier in this work. This confirms that MB-II can provide reasonable templates for intrinsic alignment models to be used in real data analysis.

## 8.3 Predictions for future weak lensing surveys

Using the SDSS  $r$ -band luminosity of galaxies in the simulation, we can make predictions for the  $w_{\delta+}$  correlation function for upcoming surveys. However, we do not separate the galaxies by their color. So, the IA signals shown here also include the type dependence. Here we focus on  $w_{\delta+}$  rather than  $w_{g+}$  since the intrinsic alignments contamination of cosmic shear signals is caused by the entire matter density field. In the left panel of Fig. 22, we plotted the  $w_{\delta+}$  correlation function for galaxy samples selected on the basis of a luminosity threshold with increasing comoving abundance at redshifts  $z = 0.3$  and  $0.6$ . Our results suggest that the amplitude of the  $w_{\delta+}$  correlation function decreases with increasing comoving abundance at both redshifts, with the shape of the correlation function changing as well (such that the 1-halo to 2-halo transition is no longer evident for lower

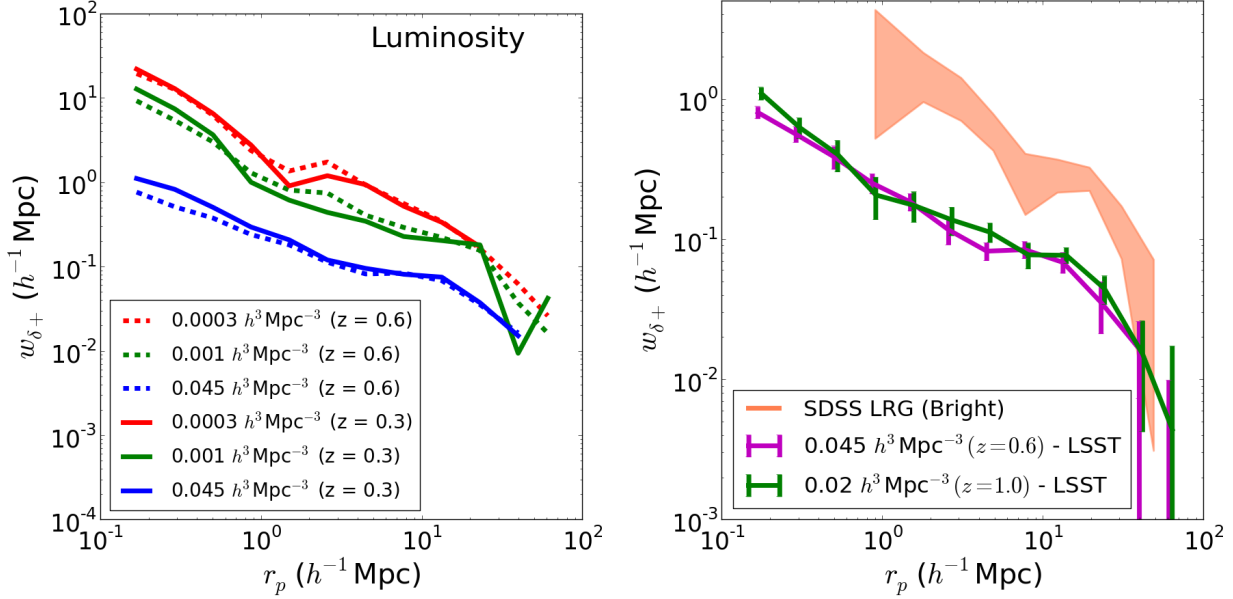


**Figure 22.** *Left:*  $w_{\delta+}$  correlation function at redshifts  $z = 0.6$  and  $0.3$  for galaxies selected by a luminosity threshold to match three values of comoving abundance as labeled on the plot. *Right:* Prediction of  $w_{\delta+}$  for galaxies that will be used for lensing in the LSST survey, made by matching the estimated comoving abundances at  $z = 1.0$  and  $z = 0.6$ . The shaded regions show jackknife errorbars.

luminosity samples, perhaps because they occupy host halos with a wide range of masses).

In the right panel of Fig. 22, we show the  $w_{\delta+}$  signals at  $z = 0.6$  and  $z = 1.0$  that help us to predict the intrinsic alignments for the galaxies that will be used to measure lensing in the upcoming LSST survey. At redshift  $z = 1.0$ , the comoving abundance of  $0.02 (h^{-1}\text{Mpc})^{-3}$  corresponds to the estimated number density of galaxies in the LSST. Similarly, at redshift  $z = 0.6$ , the estimated comoving abundance is  $0.045 (h^{-1}\text{Mpc})^{-3}$ . The galaxy number densities mentioned here are based on the results from Chang et al. (2013). From the observational measurements of intrinsic alignments using SDSS LRGs (Fig. 21), we know the value of  $w_{g+}$  which would be a good match to the signal obtained from a luminosity based comoving number density threshold of  $3 \times 10^{-4} (h^{-1}\text{Mpc})^{-3}$  (left panel of Fig. 22). For galaxies in the LSST sample, our results predict that the intrinsic alignments decrease by a factor of  $\sim 18$  for scales below  $1 h^{-1}\text{Mpc}$ . At large scales, based on the NLA model fits tabulated in Appendix A, we predict that the amplitude of the signal decreases by a factor of  $\sim 5$  at  $z = 0.6$  compared to the measured signal using LRGs.

Fig. 23 shows the evolution of NLA amplitude  $A_I$ , for different samples defined by mass threshold and comoving abundance. We observe clear evolution with mass and luminosity with more massive and luminous objects having stronger alignments. We also observe mild evolution in redshift which is inconsistent with NLA assumption that intrinsic alignments are setup at time of galaxy formation, if we assume that all our galaxies formed at  $z \gg 1$ . This assumption is however likely to break down over the broad redshift and mass range of our sample, due to growth of structure as well as dynamical evolution of galaxies which will bring the intrinsic alignments signal down, consistent with our results. As in Sec. 8.1, to quantify the luminosity and redshift

**Table 2.** Results of fitting different parameters (for mass and luminosity threshold samples only) to find their mass and luminosity evolution (Eq. 20 and 19). Different columns are the parameters that go into Eq. (20) and (19) while different rows are for different intrinsic alignments model parameters, with  $A_I$  being the NLA amplitude,  $P_A$  and  $P_I$  are power law fits (Eq. 18) to  $w_{g+}$  and  $P_A^\delta$  and  $P_I^\delta$  are power law fits to  $w_{\delta+}$ .

Parameter	$A$	$\alpha_M$	$\alpha_L$	$\alpha_z$
$A_I$	$7.7 \pm 0.5$	$0.35 \pm 0.03$	$0.48 \pm 0.03$	$0.69 \pm 0.16$
$P_A$	$0.65 \pm 0.04$	$0.57 \pm 0.03$	$0.7 \pm 0.04$	$-0.2 \pm 0.2$
$P_I$	$-0.42 \pm 0.05$	$-0.09 \pm 0.06$	$0.1 \pm 0.09$	$0.1 \pm 0.3$
$P_A^\delta$	$1.23 \pm 0.12$	$0.53 \pm 0.04$	$0.58 \pm 0.04$	$-1.0 \pm 0.2$
$P_I^\delta$	$-1.05 \pm 0.06$	$0.14 \pm 0.02$	$0.11 \pm 0.02$	$0.0 \pm 0.1$

evolution of intrinsic alignments amplitude we fit a power law defined in Eq. (19) to luminosity threshold samples and a similar power law in average mass and redshift as defined in Eq. (20) to mass threshold samples.

$$A_I = A \left( \frac{\langle M \rangle}{10^{13} h^{-1} M_\odot} \right)^{\alpha_M} (1+z)^{\alpha_z} \quad (20)$$

Since  $A$  and  $\alpha_z$  are same for both luminosity and mass threshold samples we fit both luminosity and mass threshold samples simultaneously to get all the parameters. Parameters are given in Table 2. We note that our samples defined by threshold cuts are correlated and hence the values given in Table 2 should not be directly compared with observational results, where samples are usually defined in luminosity or mass bins. The purpose of our fits given here is to give scaling relations for overall expected intrinsic alignments for sources that will be used to measure lensing in surveys like LSST and Euclid, for which the source samples will likely be derived from taking most of the galaxies above some flux cut.

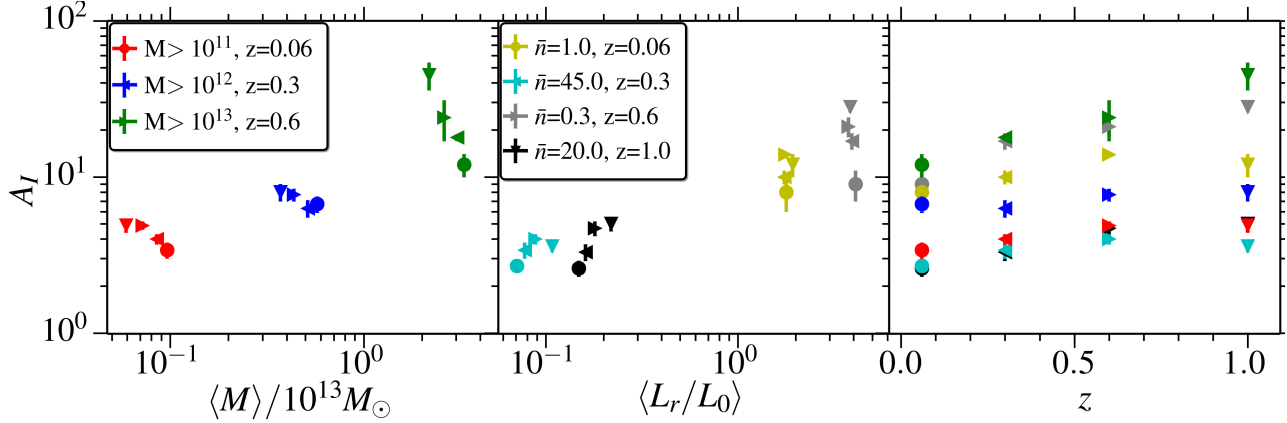


**Figure 23.** NLA amplitude,  $A_I$ , as a function of different sample properties. The horizontal axis indicates the average mass, luminosity or redshift of different samples. Points are colored by sample definition: comoving abundance ( $\bar{n}$ ) in units of  $10^{-3}h^3\text{Mpc}^{-3}$  based on a luminosity threshold, or the mass threshold of the sample (not average mass), while markers are set according to the redshift.

## 9 CONCLUSIONS

In this paper, we used the MB-II cosmological hydrodynamic simulation to study the intrinsic alignments of galaxies using the Ellipticity-Direction (ED) and the projected shape correlation function ( $w_{g+}$ ). We are able to directly measure the shapes of the stellar matter component of the galaxies and use these to estimate the two-point correlation functions which can be compared with intrinsic alignment measurements from observations. The use of hydrodynamic simulations, which include the physics of galaxy formation, has an advantage over  $N$ -body simulations in that we do not have to make assumptions about the occupation of halos with galaxies and their alignments with the host halo. We also have information on the luminosities of galaxies in the simulation, which is useful for comparisons with observations and making predictions of intrinsic alignments for upcoming surveys.

It is necessary to adopt a definition for the shapes of dark matter and stellar matter components in subhalos. We investigated the variation in the distribution of axis ratios of shapes obtained using iterative and non-iterative forms of the unweighted and reduced inertia tensor. The axis ratios and orientations of the shapes obtained using unweighted iterative and non-iterative inertia tensor are very similar. For comparison with observations, it might be useful to use the reduced form of inertia tensor which gives more weight to particles in the inner regions of a subhalo. The non-iterative reduced inertia tensor produces shapes that are biased towards being very spherical and hence is not considered. The axis ratios of shapes defined by dark matter subhalos obtained using the iterative reduced inertia tensor have slightly larger axis ratios when compared with those obtained using the unweighted inertia tensor, which is in agreement with the findings of Bett (2012). For shapes defined by stellar matter, the reduced inertia tensor produces shapes which are slightly more oblate.

We can also define a luminosity weighted unweighted and reduced inertia tensors for shapes of stellar matter. We concluded that the shapes obtained using the unweighted inertia tensor are similar when the star particle is weighted by its luminosity or mass. However, we observe noticeable

changes in the distribution of axis ratios for shapes obtained using the reduced form of the inertia tensor when we weight each particle by its luminosity. This is not surprising, as it indicates that the mass to light ratio is not constant in the inner regions of galaxy, which is expected. However, our results suggest this effect of luminosity-weighting does not affect the intrinsic alignment signals which are consistent with the ED and  $w_{g+}$  determined using shapes from mass-weighted inertia tensor.

To investigate the color dependence of intrinsic alignments, the galaxies in the simulation are roughly divided into red and blue types by choosing a median value of the rest-frame color,  $M_u - M_r$ . By comparing the  $w_{g+}$  correlation function for red and blue galaxies, we concluded that there is no significant difference in the ED and  $w_{g+}$  correlation functions for red and blue galaxies.

We measured the dependence of the two-point correlation functions, ED (position angle statistic) and  $w_{g+}$  (projected shape correlation function), on the mass and redshift. The  $w_{g+}$  correlation function is more relevant for comparison with many observational results and for contamination of upcoming weak lensing measurements by intrinsic alignments, given that it includes the overall galaxy shape. For both ED and  $w_{g+}$ , the amplitude of the correlation function is smaller for shapes defined by the reduced form of the inertia tensor. By plotting the correlation functions for galaxy samples selected in the mass bins,  $10^{11-12}h^{-1}M_\odot$ ,  $10^{12-13}h^{-1}M_\odot$  and  $10^{13-15}h^{-1}M_\odot$ , we concluded that the amplitude of the correlation function increases strongly with increasing mass. We also consider the redshift dependence of ED and  $w_{g+}$  correlation functions. For the ED correlation function, the amplitude of the correlation function decreases at low redshifts, which indicates that the shape defined by the stellar component tends to get slightly less correlated with the density field traced by subhalos. Our findings for the mass and redshift dependence of ED correlation function using the shapes of stellar matter are similar to the conclusions of Lee et al. (2008) based on  $N$ -body simulations. However, we do not notice a significant redshift dependence for the  $w_{g+}$  correlation function for fixed mass threshold samples.

The simulation also allows us to directly study the intrinsic alignment in centrals and satellite galaxies, as it is possible to split our subhalos into centrals and satellites. Previously, the intrinsic alignments in centrals and satellites has been modeled analytically using the halo model (Schneider & Bridle 2010). Here, we concluded that in low mass galaxies, the satellites have larger intrinsic alignment when compared to centrals at small scales (i.e., in the language of the halo model, the satellite galaxies have a stronger one-halo term than the centrals). At large scales, the intrinsic alignment signal for satellite galaxies goes down and is smaller than those for central galaxies (centrals have a larger two-halo term than satellites). We do not observe statistically significant differences in the intrinsic alignments of centrals and satellites in more massive galaxies.

We also fit non-linear alignment model (NLA) in the range  $6h^{-1}\text{Mpc} < r_p < 25h^{-1}\text{Mpc}$  and study the evolution of with mass, luminosity and redshift. The NLA amplitude  $A_I$  increases with mass and luminosity, qualitatively consistent with LRGs observations though our scalings are different from LRGs observations, possibly due to our focus on lower luminosity galaxies. We also fit a simple power law model to study intrinsic alignments at small scales, and observe that intrinsic alignments signal gets lower and more flattened as we go to lower mass and luminosities. We observe that intrinsic alignments get more flattened for  $w_{g+}$  as compared to  $w_{\delta+}$ , which implies that sub halos don't allow a fair measurement of intrinsic alignments signal at small scales. This has important implications for observations, where we can only use galaxies to trace the density field.

Finally, we are able to make predictions for the intrinsic alignments for upcoming surveys at redshifts  $z = 1.0$  and  $z = 0.6$  by calculating the  $w_{\delta+}$  correlation function (cross-correlation of projected shapes with density field traced by dark matter particles). For these predictions, we select galaxy samples based on a threshold in luminosity such that the comoving abundance matches the expected number density of galaxies at the given redshifts. We concluded that, as expected, the amplitude of  $w_{\delta+}$  correlation decreases as we go to larger comoving abundances. This result is important as we already have the observationally measured result for  $w_{g+}$  using data from the SDSS LRG sample. Using our results from simulation, we predict that for galaxies that will be used to measure lensing in the LSST survey, the IA signal decreases by a factor of  $\sim 5$ – $18$  depending on the radial separation (from  $\sim 30$  down to  $\sim 0.5h^{-1}\text{Mpc}$ ) compared to the measured value for LRGs. This differs from the conclusion of Codis et al. (2014), where they detected no intrinsic alignment signal in their sample of reddest galaxies at  $z = 1.2$ . The difference can be due to the fact that Codis et al. (2014) define shapes with a spin statistic which is suitable for blue galaxies. As mentioned in their paper, spins do not fully capture the shape of a galaxy or the effects of intrinsic alignments on the two-point shear statistics. It is also to be noted that their hydrodynamics is implemented based on AMR code. As our approach is based on SPH, it will be interesting to directly compare the intrinsic alignments of galaxies using a similarly defined observable to understand the differences due to numerical implementation.

In future work, we will compare the results of our two-point correlation function with predictions from a dark mat-

ter only simulation run with the same initial conditions, in order to understand the importance of the physics of galaxy formation and processes such as feedback on the intrinsic alignments. We will also try to apply additional post-processing techniques to match the color of galaxies in our simulation to those from observational results. However, the results in this work suggest that high-resolution and large-volume SPH simulations such as MB-II will be a powerful tool for predicting and mitigating intrinsic alignments in future weak lensing surveys.

## ACKNOWLEDGMENTS

We thank Benjamin Joachimi, Alina Kiessling, Cristobál Sifón, and Jonathan Blazek for providing helpful feedback on this work. RM's work on this project is supported in part by the Alfred P. Sloan Foundation. The simulations used in this work were run on NSF XSEDE HPC facilities at NICS. We acknowledge support from Moore foundation which enabled us to perform the data analysis at the McWilliams Center of Cosmology at CMU. TDM has been funded by the National Science Foundation (NSF) PetaApps, OCI-0749212 and by NSF AST-1009781 and ACI-1036211.

## REFERENCES

- Agustsson I., Brainerd T. G., 2010, *ApJ*, 709, 1321  
 Albrecht A., Bernstein G., Cahn R., Freedman W. L., Hewitt J., Hu W., Huth J., Kamionkowski M., Kolb E. W., Knox L., Mather J. C., Staggs S., Suntzeff N. B., 2006, *ArXiv Astrophysics e-prints*  
 Allgood B., Flores R. A., Primack J. R., Kravtsov A. V., Wechsler R. H., Faltenbacher A., Bullock J. S., 2006, *MNRAS*, 367, 1781  
 Benabed K., van Waerbeke L., 2004, *Phys.Rev.D*, 70, 123515  
 Bernstein G., Jain B., 2004, *ApJ*, 600, 17  
 Bett P., 2012, *MNRAS*, 420, 3303  
 Blazek J., Mandelbaum R., Seljak U., Nakajima R., 2012, *JCAP*, 5, 41  
 Blazek J., McQuinn M., Seljak U., 2011, *JCAP*, 5, 10  
 Brainerd T. G., 2005, *ApJ*, 628, L101  
 Bridle S., King L., 2007a, *New Journal of Physics*, 9, 444  
 Bridle S., King L., 2007b, *New Journal of Physics*, 9, 444  
 Bryan S. E., Kay S. T., Duffy A. R., Schaye J., Dalla Vecchia C., Booth C. M., 2013, *MNRAS*, 429, 3316  
 Catelan P., Kamionkowski M., Blandford R. D., 2001, *MNRAS*, 320, L7  
 Chang C., Jarvis M., Jain B., Kahn S. M., Kirkby D., Connolly A., Krughoff S., Peng E.-H., Peterson J. R., 2013, *MNRAS*, 434, 2121  
 Chisari N. E., Dvorkin C., 2013, *JCAP*, 12, 29  
 Codis S., Gavazzi R., Dubois Y., Pichon C., Benabed K., Desjacques V., Pogosyan D., Devriendt J., Slyz A., 2014, *ArXiv e-prints*  
 Croft R. A. C., Metzler C. A., 2000, *ApJ*, 545, 561  
 Davis M., Efstathiou G., Frenk C. S., White S. D. M., 1985, *ApJ*, 292, 371

- Deason A. J., McCarthy I. G., Font A. S., Evans N. W., Frenk C. S., Belokurov V., Libeskind N. I., Crain R. A., Theuns T., 2011, *MNRAS*, 415, 2607
- Di Matteo T., Khandai N., DeGraf C., Feng Y., Croft R. A. C., Lopez J., Springel V., 2012, *ApJ*, 745, L29
- Dong X., Lin W., Kang X., Wang Y. O., Dutton A. A., Macciò A. V., 2014, *ArXiv e-prints*
- Dubois Y., Pichon C., Welker C., Le Borgne D., Devriendt J., Laigle C., Codis S., Pogosyan D., Arnouts S., Benabed K., Bertin E., Blaizot J., Bouchet F., Cardoso J.-F., Colombi S., de Lapparent V., Desjacques V., Gavazzi R., Kassin S., Kimm T., McCracken H., Milliard B., Peirani S., Prunet S., Rouberol S., Silk J., Slyz A., Sousbie T., Teyssier R., Tresse L., Treyer M., Vibert D., Volonteri M., 2014, *arXiv*, arXiv:1402.1165
- Faltenbacher A., Jing Y. P., Li C., Mao S., Mo H. J., Pasquali A., van den Bosch F. C., 2008, *ApJ*, 675, 146
- Heavens A., Refregier A., Heymans C., 2000, *MNRAS*, 319, 649
- Heymans C., White M., Heavens A., Vale C., van Waerbeke L., 2006, *MNRAS*, 371, 750
- Hinshaw G., Larson D., Komatsu E., Spergel D. N., Bennett C. L., Dunkley J., Nolte M. R., Halpern M., Hill R. S., Odegard N., Page L., Smith K. M., Weiland J. L., Gold B., Jarosik N., Kogut A., Limon M., Meyer S. S., Tucker G. S., Wollack E., Wright E. L., 2013, *ApJS*, 208, 19
- Hirata C. M., Mandelbaum R., Ishak M., Seljak U., Nichol R., Pimblet K. A., Ross N. P., Wake D., 2007, *MNRAS*, 381, 1197
- Hirata C. M., Seljak U., 2004, *Phys.Rev.D*, 70, 063526
- Hopkins P. F., Bahcall N. A., Bode P., 2005, *ApJ*, 618, 1
- Hu W., 2002, *Phys.Rev.D*, 65, 023003
- Huterer D., 2010, *General Relativity and Gravitation*, 42, 2177
- Ishak M., Hirata C. M., McDonald P., Seljak U., 2004, *Phys.Rev.D*, 69, 083514
- Jing Y. P., 2002, *MNRAS*, 335, L89
- Joachimi B., Bridle S. L., 2010, *A&A*, 523, A1
- Joachimi B., Mandelbaum R., Abdalla F. B., Bridle S. L., 2011a, *A&A*, 527, A26
- Joachimi B., Mandelbaum R., Abdalla F. B., Bridle S. L., 2011b, *A&A*, 527, A26
- Joachimi B., Schneider P., 2008, *A&A*, 488, 829
- Joachimi B., Schneider P., 2009, *A&A*, 507, 105
- Joachimi B., Semboloni E., Hilbert S., Bett P. E., Hartlap J., Hoekstra H., Schneider P., 2013, *MNRAS*, 436, 819
- Kaiser N., 1987, *MNRAS*, 227, 1
- Kang X., van den Bosch F. C., Yang X., Mao S., Mo H. J., Li C., Jing Y. P., 2007, *MNRAS*, 378, 1531
- Katz N., Weinberg D. H., Hernquist L., 1996, *ApJS*, 105, 19
- Kazantzidis S., Zentner A. R., Nagai D., 2006, in Mamon G. A., Combes F., Deffayet C., Fort B., eds, *EAS Publications Series Vol. 20 of EAS Publications Series, The Effect of Baryons on Halo Shapes*. pp 65–68
- Khandai N., Di Matteo T., Croft R., Wilkins S. M., Feng Y., Tucker E., DeGraf C., Liu M.-S., 2014, *ArXiv e-prints*
- King L. J., 2005, *A&A*, 441, 47
- Knebe A., Libeskind N. I., Knollmann S. R., Yepes G., Gottlöber S., Hoffman Y., 2010, *MNRAS*, 405, 1119
- Knebe A., Libeskind N. I., Pearce F., Behroozi P., Casado J., Dolag K., Dominguez-Tenreiro R., Elahi P., Lux H., Muldrew S. I., Onions J., 2013, *MNRAS*, 428, 2039
- Komatsu E., Smith K. M., Dunkley J., Bennett C. L., Gold B., Hinshaw G., Jarosik N., Larson D., Nolte M. R., Page L., Spergel D. N., Halpern M., Hill R. S., Kogut A., Limon M., Meyer S. S., Odegard N., Tucker G. S., Weiland J. L., Wollack E., Wright E. L., 2011, *ApJS*, 192, 18
- Kuhlen M., Diemand J., Madau P., 2007, *ApJ*, 671, 1135
- Lee J., Rey S. C., Kim S., 2014, *ApJ*, 791, 15
- Lee J., Springel V., Pen U.-L., Lemson G., 2008, *MNRAS*, 389, 1266
- Lewis A., Bridle S., 2002, *Phys.Rev.D*, 66, 103511
- Li C., Jing Y. P., Faltenbacher A., Wang J., 2013, *ApJ*, 770, L12
- Libeskind N. I., Cole S., Frenk C. S., Okamoto T., Jenkins A., 2007, *MNRAS*, 374, 16
- Mandelbaum R., Blake C., Bridle S., Abdalla F. B., Brough S., Colless M., Couch W., Croom S., Davis T., Drinkwater M. J., Forster K., Glazebrook K., Jelliffe B., Jurek R. J., Li I.-H., Madore B., Martin C., Pimblet K., Poole G. B., Pracy M., Sharp R., Wisnioski E., Woods D., Wyder T., 2011, *MNRAS*, 410, 844
- Mandelbaum R., Hirata C. M., Ishak M., Seljak U., Brinkmann J., 2006, *MNRAS*, 367, 611
- Nierenberg A. M., Auger M. W., Treu T., Marshall P. J., Fassnacht C. D., Busha M. T., 2012, *ApJ*, 752, 99
- Okumura T., Jing Y. P., Li C., 2009, *ApJ*, 694, 214
- Pereira M. J., Bryan G. L., Gill S. P. D., 2008, *ApJ*, 672, 825
- Sales L., Lambas D. G., 2004, *MNRAS*, 348, 1236
- Schneider M. D., Bridle S., 2010, *MNRAS*, 402, 2127
- Schneider M. D., Cole S., Frenk C. S., Kelvin L., Mandelbaum R., Norberg P., Bland-Hawthorn J., Brough S., Driver S., Hopkins A., Liske J., Loveday J., Robotham A., 2013, *MNRAS*, 433, 2727
- Schneider M. D., Frenk C. S., Cole S., 2012, *JCAP*, 5, 30
- Sifón C., Hoekstra H., Cacciato M., Viola M., Köhlinger F., van der Burg R., Sand D., Graham M. L., 2014, *ArXiv e-prints*
- Singh S., Mandelbaum R., More S., 2014, *ArXiv e-prints*
- Springel V., Di Matteo T., Hernquist L., 2005, *MNRAS*, 361, 776
- Springel V., Hernquist L., 2003, *MNRAS*, 339, 289
- Springel V., White S. D. M., Tormen G., Kauffmann G., 2001, *MNRAS*, 328, 726
- Takada M., White M., 2004, *ApJ*, 601, L1
- Tenneti A., Mandelbaum R., Di Matteo T., Feng Y., Khandai N., 2014, *MNRAS*, 441, 470
- Vogelsberger M., Genel S., Springel V., Torrey P., Sijacki D., Xu D., Snyder G., Bird S., Nelson D., Hernquist L., 2014, *Nature*, 509, 177
- Vogelsberger M., Genel S., Springel V., Torrey P., Sijacki D., Xu D., Snyder G., Nelson D., Hernquist L., 2014, *MNRAS*, 444, 1518
- Wang W., Sales L. V., Henriques B. M. B., White S. D. M., 2014, *MNRAS*, 442, 1363
- Wang Y. O., Lin W. P., Kang X., Dutton A., Yu Y., Macciò A. V., 2014, *ApJ*, 786, 8
- Weinberg D. H., Mortonson M. J., Eisenstein D. J., Hirata C., Riess A. G., Rozo E., 2013, *Phys.Rep.*, 530, 87
- Yang X., van den Bosch F. C., Mo H. J., Mao S., Kang X., Weinmann S. M., Guo Y., Jing Y. P., 2006, *MNRAS*, 369,

1293

Zhang P., 2010, ApJ, 720, 1090

## APPENDIX A: FITTING RESULTS

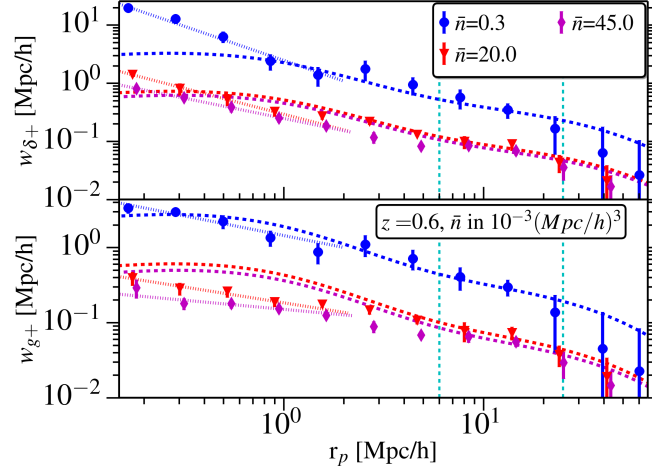
Here we present results of fitting the NLA and power law models to different samples for which  $w_{g+}$  and  $w_{\delta+}$  were measured. These are helpful to produce IA signals that scale with mass, luminosity and transverse signals according to predictions from the MBII simulation. At linear and quasi-linear scales ( $6h^{-1}\text{Mpc} < r_p < 25h^{-1}\text{Mpc}$ ) we fit  $w_{\delta+}$  and  $w_{g+}$  simultaneously for amplitude  $A_I$  and subhalo linear bias  $b_D$  in  $w_{g+}$ .  $b_D$  values are not shown in tables but we get  $b_D$  consistent with values expected for  $\xi_{gg}$  and  $\xi_{mm}$  measurements. The power-law was fitted separately to  $w_{g+}$  and  $w_{\delta+}$  for  $r_p < 1h^{-1}\text{Mpc}$ , with two free parameters, amplitude  $P_A$  and index  $P_I$ . A subscript  $\delta$  on power-law parameters denotes a fit to  $w_{\delta+}$ . Power-law parameters evolve with mass and luminosity, with the function becoming more shallow for lower mass and luminosity. As discussed in Sec. 8.1, there are also differences in power law fits to  $w_{\delta+}$  and  $w_{g+}$ , with the function being more shallow for  $w_{g+}$ . See Sec. 8.1 for more a detailed discussion.

Table A1 presents results for different samples defined by their comoving abundance. Fig. A1 shows the intrinsic alignments signal for some of the samples at  $z = 0.6$ . The intrinsic alignments amplitude generally increases with decreasing comoving abundance, consistent with the fact that more massive and brighter objects have stronger intrinsic alignments.

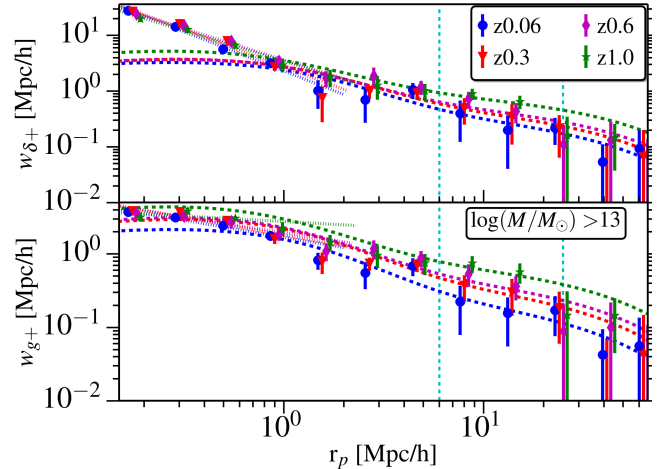
Table A2 presents results for different samples defined by subhalo mass threshold. Average subhalo mass are given for each sample. Fig. A2 shows the signal for  $M > 10^{13}h^{-1}M_{\odot}$  sample at different redshift. Samples with more massive subhalos show stronger intrinsic alignments, along with some redshift evolution as discussed in the main text.

Table A3 and Table A4 present results for satellite and central subhalos, with sample selection using different mass thresholds. Fig. A3 and Fig. A4 also show signal for some of the samples. We observe clear large scale alignments for central subhalos, also with clear mass evolution. Satellite subhalos on the other hand show very little or no alignments at large scales with  $A_I$  consistent with zero or at least much smaller than that for central subhalos at the same redshift and in the same mass range. These results are consistent with the halo model, as satellites show radial alignments within the halo and hence their large scale signal is much weaker.

Table A5 presents results for samples defined by luminosity bins. We observe evolution of intrinsic alignments with luminosity, with more luminous objects having stronger alignments and there is also some redshift evolution observed in two of the three luminosity bins. See section 8.1 for more detailed discussion.



**Figure A1.** Intrinsic alignment correlation functions,  $w_{\delta+}$  and  $w_{g+}$ , for different samples defined on the basis of comoving number density threshold, at redshift  $z = 0.6$ . There is clear evolution with number density, where samples with lower number density and hence more luminous galaxies have higher intrinsic alignments. As discussed in main text, this has important implications for future weak lensing surveys such as Euclid and LSST.



**Figure A2.** Intrinsic alignment correlation functions,  $w_{\delta+}$  and  $w_{g+}$ , for the mass threshold sample,  $M > 10^{13}h^{-1}M_{\odot}$ , at redshifts,  $z = 1.0, 0.6, 0.3,$  and  $0.06$ . We see some redshift evolution as  $w_{\delta+}$  and  $w_{g+}$  magnitude increases at higher redshift.

**Table A1.** Model fits to samples defined by a luminosity threshold, including all galaxies above some lower luminosity limit such that a given comoving abundance is achieved.  $A_I$  is the NLA model amplitude,  $P_A$  and  $P_I$  are the power law parameters. The power-law is fit separately to  $w_{g+}$  and  $w_{\delta+}$ , with superscript  $\delta$  indicating the fits to  $w_{\delta+}$ .  $\langle L/L_0 \rangle$  gives average luminosity for the sample, normalized by pivot luminosity  $L_0$ , corresponding to r-band magnitude  $M_{r,0} = -22$ .

$\bar{n}$	$z$	$A_I$	$P_A$	$P_I$	$P_A^\delta$	$P_I^\delta$	$\langle L/L_0 \rangle$
$1.0 \times 10^{-4}$	0.06	$18 \pm 2$	$2.8 \pm 0.2$	$-0.22 \pm 0.07$	$4.6 \pm 0.5$	$-1.29 \pm 0.08$	7.8
$1.0 \times 10^{-4}$	0.3	$36 \pm 4$	$3 \pm 1$	$-0.2 \pm 0.2$	$5 \pm 1$	$-1.2 \pm 0.1$	7.5
$1.0 \times 10^{-4}$	0.6	$30 \pm 10$	$2.8 \pm 0.2$	$-0.31 \pm 0.07$	$4.9 \pm 0.6$	$-1.11 \pm 0.08$	7.0
$1.0 \times 10^{-4}$	1.0	$50 \pm 10$	$3.2 \pm 0.3$	$-0.12 \pm 0.08$	$3.6 \pm 0.3$	$-1.03 \pm 0.07$	6.7
$3.0 \times 10^{-4}$	0.06	$9 \pm 2$	$1.9 \pm 0.2$	$-0.35 \pm 0.09$	$2.8 \pm 0.2$	$-1.25 \pm 0.05$	4.1
$3.0 \times 10^{-4}$	0.3	$17 \pm 2$	$1.6 \pm 0.4$	$-0.4 \pm 0.1$	$2.5 \pm 0.3$	$-1.24 \pm 0.08$	3.9
$3.0 \times 10^{-4}$	0.6	$21 \pm 3$	$1.4 \pm 0.2$	$-0.5 \pm 0.1$	$2.5 \pm 0.5$	$-1.2 \pm 0.1$	3.8
$3.0 \times 10^{-4}$	1.0	$28 \pm 2$	$1.7 \pm 0.4$	$-0.3 \pm 0.2$	$1.8 \pm 0.3$	$-1.1 \pm 0.1$	3.8
$1.0 \times 10^{-3}$	0.06	$8 \pm 2$	$0.89 \pm 0.03$	$-0.48 \pm 0.03$	$1.4 \pm 0.2$	$-1.18 \pm 0.07$	1.8
$1.0 \times 10^{-3}$	0.3	$10 \pm 1$	$0.8 \pm 0.2$	$-0.6 \pm 0.2$	$1.3 \pm 0.4$	$-1.3 \pm 0.2$	1.7
$1.0 \times 10^{-3}$	0.6	$13.9 \pm 0.3$	$0.8 \pm 0.1$	$-0.6 \pm 0.1$	$1.4 \pm 0.2$	$-1.09 \pm 0.07$	1.8
$1.0 \times 10^{-3}$	1.0	$12 \pm 2$	$0.8 \pm 0.1$	$-0.5 \pm 0.1$	$0.8 \pm 0.1$	$-1.2 \pm 0.1$	1.9
$2.0 \times 10^{-2}$	0.06	$2.6 \pm 0.3$	$0.21 \pm 0.01$	$-0.23 \pm 0.05$	$(37.0 \pm 0.9) \times 10^{-2}$	$-0.92 \pm 0.02$	$1.5 \times 10^{-1}$
$2.0 \times 10^{-2}$	0.3	$3.3 \pm 0.4$	$0.14 \pm 0.01$	$0.43 \pm 0.08$	$0.36 \pm 0.08$	$-0.8 \pm 0.2$	$1.6 \times 10^{-1}$
$2.0 \times 10^{-2}$	0.6	$4.7 \pm 0.5$	$0.18 \pm 0.01$	$-0.42 \pm 0.06$	$(28.0 \pm 0.9) \times 10^{-2}$	$-0.9 \pm 0.02$	$1.8 \times 10^{-1}$
$2.0 \times 10^{-2}$	1.0	$5.0 \pm 0.5$	$(14.9 \pm 0.8) \times 10^{-2}$	$-0.5 \pm 0.08$	$0.18 \pm 0.01$	$-0.98 \pm 0.04$	$2.2 \times 10^{-1}$
$4.5 \times 10^{-2}$	0.06	$2.7 \pm 0.2$	$0.19 \pm 0.01$	$-0.04 \pm 0.05$	$0.36 \pm 0.02$	$-0.66 \pm 0.04$	$7.1 \times 10^{-2}$
$4.5 \times 10^{-2}$	0.3	$3.4 \pm 0.4$	$0.1 \pm 0.01$	$0.5 \pm 0.2$	$0.31 \pm 0.05$	$-0.7 \pm 0.1$	$7.8 \times 10^{-2}$
$4.5 \times 10^{-2}$	0.6	$4.0 \pm 0.3$	$0.15 \pm 0.01$	$-0.2 \pm 0.1$	$(23.2 \pm 0.6) \times 10^{-2}$	$-0.7 \pm 0.02$	$8.8 \times 10^{-2}$
$4.5 \times 10^{-2}$	1.0	$3.6 \pm 0.3$	$0.11 \pm 0.01$	$-0.5 \pm 0.1$	$0.16 \pm 0.01$	$-0.73 \pm 0.06$	$1.1 \times 10^{-1}$

**Table A2.** Model fits to samples defined by mass threshold subhalo mass.  $\langle M/h^{-1}M_\odot \rangle$  is the average subhalo mass with in the sample. See Table A1 for description of different parameters.

$\log(M/h^{-1}M_\odot)$	$z$	$A_I$	$P_A$	$P_I$	$P_A^\delta$	$P_I^\delta$	$\langle M/h^{-1}M_\odot \rangle$
>11	0.06	$3.4 \pm 0.4$	$0.15 \pm 0.02$	$-0.36 \pm 0.08$	$0.2 \pm 0.04$	$-0.9 \pm 0.1$	$9.6 \times 10^{11}$
>11	0.3	$4.0 \pm 0.3$	$(14.8 \pm 0.4) \times 10^{-2}$	$-0.49 \pm 0.02$	$(26.0 \pm 0.3) \times 10^{-2}$	$(-74.0 \pm 0.7) \times 10^{-2}$	$8.5 \times 10^{11}$
>11	0.6	$4.9 \pm 0.3$	$0.14 \pm 0.02$	$-0.5 \pm 0.1$	$0.16 \pm 0.02$	$-0.98 \pm 0.08$	$7.2 \times 10^{11}$
>11	1.0	$4.9 \pm 0.5$	$(12.5 \pm 0.3) \times 10^{-2}$	$-0.6 \pm 0.03$	$(11.6 \pm 0.9) \times 10^{-2}$	$-1.1 \pm 0.05$	$5.9 \times 10^{11}$
>12	0.06	$6.7 \pm 0.8$	$0.36 \pm 0.02$	$-0.68 \pm 0.03$	$0.4 \pm 0.05$	$-1.4 \pm 0.08$	$5.7 \times 10^{12}$
>12	0.3	$6.3 \pm 0.8$	$0.39 \pm 0.04$	$-0.7 \pm 0.08$	$0.6 \pm 0.2$	$-1.2 \pm 0.2$	$5.1 \times 10^{12}$
>12	0.6	$7.7 \pm 0.7$	$0.41 \pm 0.02$	$-0.64 \pm 0.03$	$0.53 \pm 0.04$	$-1.22 \pm 0.05$	$4.3 \times 10^{12}$
>12	1.0	$8 \pm 1$	$0.41 \pm 0.04$	$-0.69 \pm 0.07$	$0.39 \pm 0.04$	$-1.35 \pm 0.07$	$3.7 \times 10^{12}$
>13	0.06	$12 \pm 2$	$1.68 \pm 0.08$	$-0.47 \pm 0.04$	$2.3 \pm 0.3$	$-1.4 \pm 0.1$	$3.3 \times 10^{13}$
>13	0.3	$17.9 \pm 0.9$	$1.8 \pm 0.4$	$-0.5 \pm 0.2$	$2.5 \pm 0.5$	$-1.3 \pm 0.1$	$3.0 \times 10^{13}$
>13	0.6	$24 \pm 7$	$1.9 \pm 0.2$	$-0.42 \pm 0.09$	$3.3 \pm 0.4$	$-1.13 \pm 0.09$	$2.6 \times 10^{13}$
>13	1.0	$45 \pm 9$	$2.7 \pm 0.5$	$-0.1 \pm 0.1$	$2.9 \pm 0.4$	$-1.1 \pm 0.1$	$2.2 \times 10^{13}$

**Table A3.** Model fits to central galaxy intrinsic alignment correlation functions.  $\langle M/h^{-1}M_\odot \rangle$  is the average subhalo mass with in the sample. See Table A1 for description of different parameters.

$\log(M/h^{-1}M_\odot)$	$z$	$A_I$	$P_A$	$P_I$	$P_A^\delta$	$P_I^\delta$	$\langle M/h^{-1}M_\odot \rangle$
$\in [10.0, 11.5]$	0.06	$3.7 \pm 0.4$	$0.09 \pm 0.02$	$0.1 \pm 0.2$	$0.17 \pm 0.04$	$1.9 \pm 0.9$	$1.3 \times 10^{11}$
$\in [10.0, 11.5]$	0.3	$4.2 \pm 0.5$	$0.1 \pm 0.01$	$0.2 \pm 0.1$	$0.19 \pm 0.02$	$0.6 \pm 0.2$	$1.3 \times 10^{11}$
$\in [10.0, 11.5]$	0.6	$4.7 \pm 0.3$	$(10.6 \pm 0.6) \times 10^{-2}$	$-0.1 \pm 0.06$	$0.14 \pm 0.03$	$(-0.0 \pm 0.1) \times 10^0$	$1.2 \times 10^{11}$
$\in [10.0, 11.5]$	1.0	$4.1 \pm 0.4$	$(8.3 \pm 0.7) \times 10^{-2}$	$-0.2 \pm 0.1$	$0.07 \pm 0.01$	$-0.4 \pm 0.1$	$1.1 \times 10^{11}$
$\in [11.5, 13.0]$	0.06	$3.1 \pm 0.8$	$0.14 \pm 0.02$	$-0.7 \pm 0.1$	$0.03 \pm 0.03$	$-2.1 \pm 0.6$	$1.3 \times 10^{12}$
$\in [11.5, 13.0]$	0.3	$4.0 \pm 0.6$	$(12.7 \pm 0.3) \times 10^{-2}$	$-0.84 \pm 0.01$	$(7.5 \pm 0.9) \times 10^{-2}$	$-1.59 \pm 0.07$	$1.2 \times 10^{12}$
$\in [11.5, 13.0]$	0.6	$5.8 \pm 0.5$	$0.13 \pm 0.03$	$-0.7 \pm 0.2$	$0.03 \pm 0.02$	$-2.1 \pm 0.3$	$1.2 \times 10^{12}$
$\in [11.5, 13.0]$	1.0	$5.5 \pm 0.8$	$0.15 \pm 0.02$	$-0.82 \pm 0.08$	$0.1 \pm 0.01$	$-1.48 \pm 0.07$	$1.1 \times 10^{12}$
$\in [13.0, 15.0]$	0.06	$11 \pm 2$	$1.6 \pm 0.1$	$-0.48 \pm 0.07$	$2.1 \pm 0.4$	$-1.5 \pm 0.1$	$3.4 \times 10^{13}$
$\in [13.0, 15.0]$	0.3	$18 \pm 1$	$1.8 \pm 0.4$	$-0.5 \pm 0.2$	$2.8 \pm 0.5$	$-1.3 \pm 0.1$	$3.1 \times 10^{13}$
$\in [13.0, 15.0]$	0.6	$24 \pm 5$	$1.7 \pm 0.3$	$-0.5 \pm 0.1$	$2.7 \pm 0.4$	$-1.2 \pm 0.1$	$2.6 \times 10^{13}$
$\in [13.0, 15.0]$	1.0	$49 \pm 9$	$2.6 \pm 0.4$	$-0.2 \pm 0.2$	$2.8 \pm 0.4$	$-1.1 \pm 0.1$	$2.2 \times 10^{13}$

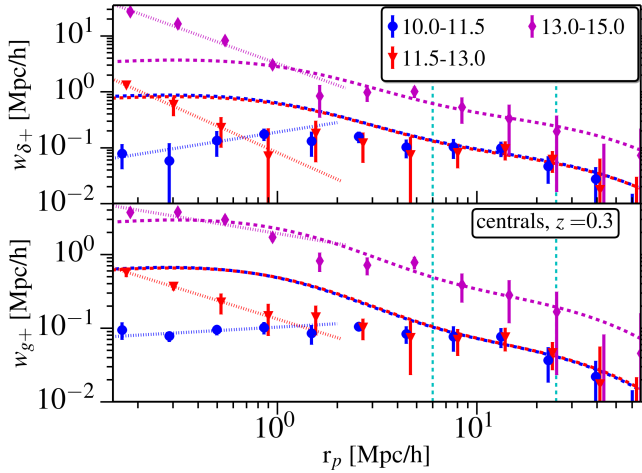
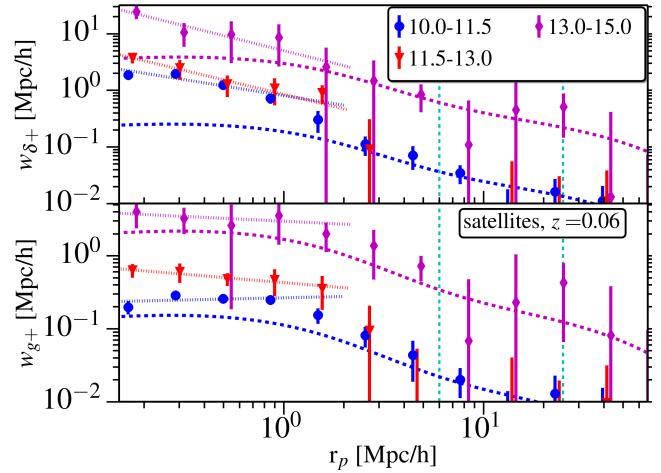


**Table A4.** Model fits to satellite galaxy intrinsic alignment correlation functions.  $\langle M/h^{-1}M_\odot \rangle$  is the average subhalo mass within the sample. See Table A1 for description of different parameters.

$\log(M/h^{-1}M_\odot)$	$z$	$A_I$	$P_A$	$P_I$	$P_A^\delta$	$P_I^\delta$	$\langle M/h^{-1}M_\odot \rangle$
$\in [10.0, 11.5]$	0.06	$0.9 \pm 0.3$	$0.26 \pm 0.03$	$0.1 \pm 0.1$	$0.8 \pm 0.2$	$-0.6 \pm 0.2$	$6.5 \times 10^{10}$
$\in [10.0, 11.5]$	0.3	$1.7 \pm 0.1$	$0.21 \pm 0.03$	$-0.25 \pm 0.09$	$0.6 \pm 0.1$	$-0.6 \pm 0.1$	$6.2 \times 10^{10}$
$\in [10.0, 11.5]$	0.6	$1.6 \pm 0.2$	$0.18 \pm 0.03$	$-0.1 \pm 0.1$	$0.34 \pm 0.07$	$-0.6 \pm 0.1$	$6.1 \times 10^{10}$
$\in [10.0, 11.5]$	1.0	$2.0 \pm 0.4$	$0.14 \pm 0.01$	$-0.3 \pm 0.1$	$0.3 \pm 0.07$	$-0.6 \pm 0.1$	$5.7 \times 10^{10}$
$\in [11.5, 13.0]$	0.06	$-1 \pm 1$	$0.42 \pm 0.03$	$-0.23 \pm 0.05$	$0.8 \pm 0.1$	$-0.8 \pm 0.1$	$1.0 \times 10^{12}$
$\in [11.5, 13.0]$	0.3	$4.1 \pm 0.7$	$(32.1 \pm 0.8) \times 10^{-2}$	$-0.57 \pm 0.02$	$0.9 \pm 0.2$	$-0.8 \pm 0.1$	$1.0 \times 10^{12}$
$\in [11.5, 13.0]$	0.6	$3 \pm 1$	$0.66 \pm 0.06$	$-0.14 \pm 0.07$	$1.5 \pm 0.2$	$-0.4 \pm 0.1$	$9.9 \times 10^{11}$
$\in [11.5, 13.0]$	1.0	$(0.0 \pm 0.3) \times 10^1$	$0.37 \pm 0.05$	$-0.2 \pm 0.1$	$0.7 \pm 0.2$	$-0.7 \pm 0.2$	$9.0 \times 10^{11}$
$\in [13.0, 15.0]$	0.06	$10 \pm 10$	$2.9 \pm 0.6$	$-0.1 \pm 0.1$	$5 \pm 2$	$-0.9 \pm 0.3$	$2.2 \times 10^{13}$
$\in [13.0, 15.0]$	0.3	$20 \pm 20$	$(0.0 \pm 0.2) \times 10^0$	$-3 \pm 2$	$(0.0 \pm 0.3) \times 10^7$	$(0.0 \pm 0.2) \times 10^6$	$1.7 \times 10^{13}$
$\in [13.0, 15.0]$	0.6	$40 \pm 30$	$5 \pm 1$	$0.8 \pm 0.5$	$11 \pm 2$	$-0.3 \pm 0.1$	$2.3 \times 10^{13}$
$\in [13.0, 15.0]$	1.0	$-40 \pm 20$	$3 \pm 1$	$0.2 \pm 0.6$	$6.3 \pm 0.3$	$-0.71 \pm 0.05$	$2.1 \times 10^{13}$

**Table A5.** Model fits to intrinsic alignments measurements for samples defined in luminosity bins. See Table A1 for description of different parameters.

$M_r$	$z$	$A_I$	$P_A$	$P_I$	$P_A^\delta$	$P_I^\delta$	$\langle L/L_0 \rangle$
$\leq -22.6$	0.06	$12 \pm 2$	$2.0 \pm 0.2$	$-0.36 \pm 0.09$	$3.1 \pm 0.3$	$-1.29 \pm 0.07$	4.5
$\leq -22.6$	0.3	$20 \pm 2$	$1.9 \pm 0.4$	$-0.3 \pm 0.1$	$3.0 \pm 0.3$	$-1.17 \pm 0.07$	4.4
$\leq -22.6$	0.6	$24 \pm 4$	$1.6 \pm 0.2$	$-0.5 \pm 0.1$	$2.7 \pm 0.5$	$-1.2 \pm 0.1$	4.1
$\leq -22.6$	1.0	$27 \pm 2$	$1.7 \pm 0.4$	$-0.3 \pm 0.2$	$1.9 \pm 0.3$	$-1.1 \pm 0.1$	3.8
$\in [-22.6, -20.3]$	0.06	$6 \pm 1$	$0.37 \pm 0.02$	$-0.66 \pm 0.04$	$0.4 \pm 0.1$	$-1.5 \pm 0.2$	$5.2 \times 10^{-1}$
$\in [-22.6, -20.3]$	0.3	$6 \pm 1$	$0.32 \pm 0.04$	$-0.7 \pm 0.1$	$0.5 \pm 0.1$	$-1.2 \pm 0.2$	$4.9 \times 10^{-1}$
$\in [-22.6, -20.3]$	0.6	$5.6 \pm 0.2$	$0.31 \pm 0.01$	$-0.62 \pm 0.02$	$0.49 \pm 0.02$	$-1.08 \pm 0.03$	$4.9 \times 10^{-1}$
$\in [-22.6, -20.3]$	1.0	$4.6 \pm 0.5$	$0.21 \pm 0.01$	$-0.73 \pm 0.04$	$0.2 \pm 0.02$	$-1.32 \pm 0.06$	$5.0 \times 10^{-1}$
$\in [-20.3, -18.0]$	0.06	$1.5 \pm 0.3$	$(14.6 \pm 0.5) \times 10^{-2}$	$-0.32 \pm 0.03$	$0.34 \pm 0.05$	$-0.72 \pm 0.09$	$6.6 \times 10^{-2}$
$\in [-20.3, -18.0]$	0.3	$2.9 \pm 0.3$	$0.16 \pm 0.01$	$-0.42 \pm 0.07$	$0.29 \pm 0.05$	$-0.8 \pm 0.1$	$6.6 \times 10^{-2}$
$\in [-20.3, -18.0]$	0.6	$4.2 \pm 0.5$	$0.13 \pm 0.02$	$-0.3 \pm 0.1$	$0.18 \pm 0.03$	$-0.7 \pm 0.1$	$6.5 \times 10^{-2}$
$\in [-20.3, -18.0]$	1.0	$3.8 \pm 0.3$	$(11.0 \pm 0.6) \times 10^{-2}$	$-0.46 \pm 0.05$	$0.15 \pm 0.02$	$-0.71 \pm 0.07$	$6.3 \times 10^{-2}$


**Figure A3.** Intrinsic alignment correlation functions,  $w_{\delta+}$  and  $w_{g+}$ , for central subhalos in different mass bins, at redshift  $z = 0.3$ . We detect both large scale and small scale intrinsic alignments for central sub halos, with more massive sub halos also showing stronger alignments. The downturn in the lowest mass bin at small scales indicates a transition to the 1-halo term.

**Figure A4.** Intrinsic alignment correlation functions,  $w_{\delta+}$  and  $w_{g+}$ , for satellite subhalos in different mass bins,  $M1$ ,  $M2$  and  $M3$ , at redshift  $z = 0.3$ . Satellites show no significant alignments at large scales, though small scale alignment is very strong, consistent with the radial alignment of satellites.